

MICROCOPY RESOLUTION TEST CHART  
NATIONAL BUREAU OF STANDARDS-1963-A

AD-A133 254

SECURITY CLASSIFICATION OF THIS PAGE (When Data Entered)

6

REPORT DOCUMENTATION PAGE		READ INSTRUCTIONS BEFORE COMPLETING FORM
1. REPORT NUMBER N00014-81-K-0718-7	2. GOVT ACCESSION NO.	3. RECIPIENT'S CATALOG NUMBER
4. TITLE (and Subtitle) DIFFRACTION TECHNIQUES	5. TYPE OF REPORT & PERIOD COVERED Technical Report	
	6. PERFORMING ORG. REPORT NUMBER	
7. AUTHOR(s) M. G. Lagally	8. CONTRACT OR GRANT NUMBER(s) N00014-81-K-0718	
9. PERFORMING ORGANIZATION NAME AND ADDRESS Board of Regents of the University of Wisconsin System, 750 University Avenue, Madison, WI 53706	10. PROGRAM ELEMENT, PROJECT, TASK AREA & WORK UNIT NUMBERS NR 629-772	
11. CONTROLLING OFFICE NAME AND ADDRESS Office of Naval Research Arlington, VA 22217	12. REPORT DATE August 30, 1983	
	13. NUMBER OF PAGES 115	
14. MONITORING AGENCY NAME & ADDRESS (if different from Controlling Office) Office of Naval Research Branch Office Chicago 536 S. Clark Street, Room 286 Chicago, IL 60605	15. SECURITY CLASS. (of this report) Unclassified	
	15a. DECLASSIFICATION/DOWNGRADING SCHEDULE	
16. DISTRIBUTION STATEMENT (of this Report) Approved for public release; distribution unlimited.		
17. DISTRIBUTION STATEMENT (of the abstract entered in Block 20, if different from Report) A		
18. SUPPLEMENTARY NOTES To be published in <u>Methods of Experimental Physics: Surfaces</u> , eds. R. L. Park and M. G. Lagally, Academic Press, NY (1984).		
19. KEY WORDS (Continue on reverse side if necessary and identify by block number) Diffraction, surfaces, LEED, RHEED, experimental methods.		
20. ABSTRACT (Continue on reverse side if necessary and identify by block number) See Table of Contents.		

DTIC ELECTED  
S OCT 5 1983  
A

DTIC FILE COPY

DD FORM 1473 1 JAN 73 EDITION OF 1 NOV 68 IS OBSOLETE S/N 0102-014-6001

SECURITY CLASSIFICATION OF THIS PAGE (When Data Entered)

83 10 04 099

OFFICE OF NAVAL RESEARCH

Contract No. N00014-81-K-0718

Project NR 629-772

TECHNICAL REPORT No. 7

DIFFRACTION TECHNIQUES

by

M. G. Lagally  
Department of Metallurgical and Mineral Engineering  
and Materials Science Center  
University of Wisconsin-Madison  
Madison, Wisconsin 53706

August 30, 1983

To be published in  
Methods of Experimental Physics: Surfaces  
eds. R. L. Park and M. G. Lagally, Academic Press, NY (1984)

Reproduction in whole or in part is permitted  
for any purpose of the United States Government

DISTRIBUTION OF THIS DOCUMENT IS UNLIMITED



Table of Contents

I.	Introduction	1
II.	Elements of Diffraction Theory	3
	A. Diffraction From Surfaces	7
	B. Surface Defects	10
	1. Clean Surfaces	10
	2. Overlayers	17
III.	The Measurement of Diffracted-Intensity Distributions	22
	A. Sensitivity	23
	B. Resolving Power	24
IV.	Surface Crystallography Measurements	35
	A. Diffraction Patterns	35
	B. Equilibrium Position Determinations	35
	C. Structural Defects	41
	D. Thermodynamics and Kinetics	47
V.	Instrumentation and Sample Preparation	51
	A. Electron Guns	51
	B. Detectors	54
	C. Goniometers	62
	D. Sample Preparation	63
VI.	Representative Experimental Results	66
VII.	Conclusions	70
VIII.	Acknowledgements	72
	References	73
	Figure Captions	80

I. Introduction

Probably the most important of all surface analysis techniques are those that give information about the surface structure. Apart from secondary and thermionic emission, they are also the oldest. In December 1927, the following appeared as the introductory paragraphs in an article in *Physical Review*: "The investigation reported in this paper was begun as the result of an accident that occurred in this laboratory in April 1927. At that time, we were continuing an investigation. . . of the distribution in angle of electrons scattered by a target of polycrystalline nickel. During the course of this work a liquid-air bottle exploded at a time when the target was at a high temperature; the experimental tube was broken, and the target heavily oxidized by the intruding air. The oxide was eventually reduced and a layer of the target removed by vaporization, but only after prolonged heating at various high temperatures in hydrogen and in vacuum. When the experiments were continued it was found that the distribution-in-angle of the scattered electrons had completely changed. . . . The most striking characteristic of [the observed strong beams in particular directions] is the one-to-one correspondence [that they] bear to the same beams that would be found issuing from the same crystal if the incident beam were a beam of x-rays".(1)

Thus was the diffraction of electrons discovered. It may seem that little has changed since that first low-energy electron diffraction (LEED) experiment. Vacuum accidents still happen (perhaps with less serendipitous returns) and Ni has continued to be a favorite material for LEED studies. More remarkable, however, is that most of the important

features of the diffraction of electrons were recognized within a few years of the Davisson-Germer paper.<sup>(1)</sup> Since then, there have been considerable refinements in the basic ideas (brought about especially by the advent of ultrahigh vacuum), many applications, and better methods of analysis and quantification, as well as a periodic rediscovery of the fundamental ideas. There has been an expansion to other energy ranges, leading to the acronyms MEED (medium-energy electron diffraction) and RHEED (reflection high-energy electron diffraction). There have been considerable instrumental developments,<sup>(2-6)</sup> especially in recent years,<sup>(7-12)</sup> as it became apparent that the resolving power and sensitivity of existing instruments were insufficient to meet the goals of the experiments being undertaken. There have been theoretical developments, particularly in the construction of dynamical theories of low-energy electron diffraction,<sup>(13-17)</sup> but also in the analysis of structural defects<sup>(18-27)</sup>. And finally, there has been the growing recognition that crystallographic information is necessary to interpret the output of other surface spectroscopies, with the consequence that a LEED or RHEED capability has become standard equipment on more or less all experimental systems for surface research.

This chapter is an attempt to summarize, in a tutorial fashion, the most important experimental aspects of surface-sensitive diffraction. The desired result is that the reader will understand enough of the essentials to set up a diffraction experiment and interpret the results. It is not a compendium of recent, or even the most important, results of surface crystallography. Thus no attempt has been made to develop a comprehensive list of references; only those most germane to the goal stated above are

included. A number of reviews exist on various aspects of surface crystallography.<sup>(16,17,25-46)</sup> Especially the older ones are well worth reading to obtain a clear overview of diffraction techniques.

We begin with the motivation for doing diffraction, namely to learn about the atomic structure of surfaces, by discussing the general types of surface crystallographic information that can be obtained with a surface-sensitive diffraction technique. This is done in the context of simple diffraction theory. After the establishment of this framework in Section II, the rest of this chapter will concentrate on experimental aspects of diffraction. Two major techniques, LEED and RHEED, will be discussed. The emphasis will be on LEED because of the much greater activity historically and still today in LEED. However, much of the description of LEED applies as well to RHEED. Additional discussion of RHEED will focus on those experimental aspects that are unique, different, or of particular value in certain experiments. Section III will deal with measurements of diffracted intensity distributions in general terms, including a discussion of resolving power. In Section IV specific measurements are discussed and in Sec. V the instrumentation required to carry out these measurements is described. Some representative results are given in Section VI and a brief conclusion follows Section VII.

## II. Elements of Diffraction Theory

In almost all interpretations of surface electronic, chemical, or transport properties, the positions of atoms, their separations, their deviations from perfect periodicity, or the positions of their nearest or next-nearest neighbors are necessary inputs. These properties are ideally

probed with a diffraction technique. If one considers the elastic scattering of radiation with momentum  $\underline{k}_0$  from a rigid cubic crystal with lattice points

$$\underline{r}_j = m_1 \underline{a} + m_2 \underline{b} + m_3 \underline{c}, \quad (1)$$

where  $m_1, m_2, m_3$  are integers, with atoms located within each unit cell at positions

$$\underline{r}_n = u_n \underline{a} + v_n \underline{b} + w_n \underline{c}, \quad (2)$$

where  $u_n, v_n, w_n$  are fractions, the amplitude at a given momentum transfer  $\underline{s} = \underline{k} - \underline{k}_0$  is given by

$$A(\underline{s}) = \sum_{j,n} f_n(\theta, E) \exp [i \underline{s} \cdot (\underline{r}_j + \underline{r}_n)]. \quad (3)$$

The sum is over lattice sites  $j$  and the atoms  $n$  within a unit cell.

$f_n(\theta, E)$  is the atomic scattering factor of the  $n$ 'th atom, where  $\theta$  is half the scattering angle and  $E$  is the energy of the radiation. Separating the sums,

$$A(\underline{s}) = F(\theta, E) \sum_j \exp [i \underline{s} \cdot \underline{r}_j], \quad (4)$$

where

$$F(\theta, E) = \sum_n f_n(\theta, E) \exp [i \underline{s} \cdot \underline{r}_n] \quad (5)$$

is the structure factor. The intensity then is

$$I(\underline{s}) = A(\underline{s}) A^*(\underline{s}) = |F(\theta, E)|^2 \mathcal{I}(\underline{s}), \quad (6)$$

where  $\mathcal{I}(\underline{s})$  is called the interference function.  $\mathcal{I}(\underline{s})$  can be visualized using the concept of the reciprocal lattice. For a three-dimensional infinite crystal, the reciprocal lattice is a three-dimensional array of points whose positions are given by the reciprocal-lattice vectors  $\underline{G}_{hkl}$ , where  $|\underline{G}_{hkl}| = \pi / d_{hkl}$  and  $d_{hkl}$  is the distance between  $(hkl)$  planes. The interference function is periodic with  $\underline{G}_{hkl}$  and for an arbitrary momentum transfer  $\underline{s}$  can be written in terms of  $\underline{G}_{hkl}$  and the deviation parameter  $\underline{\xi} = \underline{s} - \underline{G}_{hkl}$ . For a crystal with dimensions  $N_1 a, N_2 b,$  and  $N_3 c$ , where  $a, b, c$ , are the lattice constants,

$$\mathcal{I}(\underline{G}_{hkl} + \underline{\xi}) = \frac{\sin^2 1/2 N_1 (\underline{G}_{hkl} + \underline{\xi}) \cdot \underline{a}}{\sin^2 1/2 (\underline{G}_{hkl} + \underline{\xi}) \cdot \underline{a}} \frac{\sin^2 1/2 N_2 (\underline{G}_{hkl} + \underline{\xi}) \cdot \underline{b}}{\sin^2 1/2 (\underline{G}_{hkl} + \underline{\xi}) \cdot \underline{b}} \times \frac{\sin^2 1/2 N_3 (\underline{G}_{hkl} + \underline{\xi}) \cdot \underline{c}}{\sin^2 1/2 (\underline{G}_{hkl} + \underline{\xi}) \cdot \underline{c}} \quad (7)$$

$\mathcal{I}(\underline{G}_{hkl} + \underline{\xi})$  has its maximum value,  $\mathcal{I}(\underline{G}_{hkl})$ , when  $\underline{\xi} = 0$ , i.e., when  $\underline{s}$  satisfies the Laue conditions

$$\underline{s} = \underline{G}_{hkl}$$

or

$$\underline{s} \cdot \underline{a} = 2\pi h, \quad \underline{s} \cdot \underline{b} = 2\pi k, \quad \underline{s} \cdot \underline{c} = 2\pi l, \quad (8)$$



where  $h, k, l$  are integers. The maxima in the interference function have heights proportional to  $(N_1 N_2 N_3)^2$  and widths in three orthogonal directions in  $\underline{s}$  space proportional to  $1/N_1 a, 1/N_2 b,$  and  $1/N_3 c$ .

A useful representation of diffraction from a lattice is in terms of its reciprocal lattice and the Ewald construction. The Ewald sphere gives simply the conservation of energy for elastic scattering, i.e.,  $\lambda_{in} = \lambda_{out}$  or  $|\underline{k}_0| = |\underline{k}|$ , where  $\lambda$  and  $\underline{k}$  are respectively the electron wavelength and momentum. The superposition of the Ewald sphere onto the reciprocal lattice shows conservation of momentum as well as energy in the form of the Laue conditions  $\underline{s} = \underline{G}_{hkl}$ . The diffracted-intensity distribution in angle at constant energy is then given by the intersection of the Ewald sphere with the reciprocal lattice. The Ewald construction for penetrating radiation is shown in Fig. 1a for the energy and diffraction geometry appropriate for LEED. An incident beam with a perfectly defined momentum is assumed and, as a result, the Ewald sphere is perfectly sharp. Figure 1b shows the situation for penetrating radiation for the energies and diffraction geometry appropriate for RHEED or grazing-angle x-ray diffraction. The relationship between the lengths of the  $\underline{k}$  vectors and the reciprocal-lattice vector is appropriate respectively for LEED with 150 eV electrons and RHEED with 10,000 eV electrons. As the energy or angle is varied, diffraction spots will appear or disappear, but only one or several diffracted beams will be excited and hence visible in the diffraction pattern at one set of diffraction conditions.

#### A. Diffraction from Surfaces

For an adsorbed monolayer (or in any case where a phase is only one atomic layer thick) it is easy to demonstrate that the reciprocal lattice becomes a set of rods normal to the plane of the layer. In Eq. (7)  $N_3 = 1$  and the third term equals one, implying that the interference function has a constant value for all values of  $(\underline{G}_{hkl} + \underline{s}) \cdot \underline{c}$ . Figure 2 shows the Ewald constructions corresponding to LEED and RHEED for this case. It is evident that now many more diffracted beams are excited for any diffraction geometry, and that they will remain excited as the energy or diffraction geometry is varied.

Intermediate between the limit of an infinite three-dimensional crystal and an infinite two-dimensional crystal is one that has a finite dimension in the third direction. This situation is approximated for any infinite three-dimensional crystal if the radiation used for the diffraction experiment does not penetrate the sample to very large depths. This must clearly be the case for all techniques that are surface-sensitive, but the limited penetration is achieved in different ways. Under optimum conditions only one or two atomic planes make a significant contribution to the diffracted intensity.

The interference function for a crystal that is artificially limited in the  $z$ -direction by an exponentially decreasing magnitude of scattering density can be described by defining<sup>(47)</sup> an attenuation coefficient,  $\alpha$ , such that

$$\alpha = \frac{A_{n+1}}{A_n}, \quad (9)$$

where  $A_n$  is the amplitude scattered by the  $n$ 'th atomic plane. The total

scattered amplitude is then

$$A(\xi) = \sum_{j,n} F_j(\theta, E) \alpha^{n_j} \exp[i\xi \cdot r_j], \quad (10)$$

where  $n_j$  specifies the plane containing the  $j$ 'th atom. The interference function becomes

$$I(\xi_{hk1}, \xi_{\parallel}) = |F(\theta, E)|^2 \frac{\sin^2 \frac{1}{2} N_1 (\xi_{hk1}, \xi_{\parallel}) \cdot a}{\sin^2 \frac{1}{2} (\xi_{hk1}, \xi_{\parallel}) \cdot a} \frac{\sin^2 \frac{1}{2} N_2 (\xi_{hk1}, \xi_{\parallel}) \cdot b}{\sin^2 \frac{1}{2} (\xi_{hk1}, \xi_{\parallel}) \cdot b} \times \frac{1}{1 + \alpha^{-2} - 2\alpha \cos(\xi_{hk1}, \xi_{\parallel}) \cdot c}. \quad (11)$$

Unlike a grating with a finite number of lines,  $N_3$ , which produces  $N_3 - 2$  intermediate interference maxima, such an attenuated grating produces only broad maxima that are smoothly connected. This implies that the reciprocal lattice consists of neither points (3-D) nor "rods" (2-D) but rather of "elongated points" or "cigars" in the  $c^*$  direction. The interference function thus is modulated. This modulation can be expressed in terms of the mean free path for inelastic scattering,  $\lambda_{inel}$ , by<sup>(34,47)</sup>

$$\alpha = \exp \left[ \frac{c}{2\lambda_{inel}} \left( \frac{1}{\cos \theta_0} - \frac{1}{\cos \theta} \right) \right], \quad (12)$$

where  $\theta_0$  and  $\theta$  are respectively the angles the incident and diffracted beams make with the surface normal. Because the last term in Eq. (11) never goes to zero for attenuations typical of surface-sensitive diffraction techniques, it is customary to describe the reciprocal lattice as a set of rods, as for a single layer, keeping in mind however that the intensity along these rods is modulated with a period that reflects the interlayer distance perpendicular to the surface. This is illustrated in Fig. 3.

The limited penetration of the radiation in surface-sensitive diffraction techniques is achieved in different ways. At the energies used in LEED, 10-1000 eV, the cross sections for both elastic and inelastic scattering are so large that the penetration of the beam is very small. The inelastic and elastic scattering cross sections have approximately the same magnitude, of the order of several  $\text{\AA}^2$ . The sensitivity of LEED to the surface is in large part due to the strong inelastic scattering. The inelastic mean free path of electrons, i.e., the distance an electron beam travels in a crystal before inelastic collisions reduce the beam intensity by a factor of  $1/e$ , is plotted as a function of energy in Fig. 4. In the energy range of 100 eV, the inelastic mean free path may be as little as 4 $\text{\AA}$ . Because of the strong elastic scattering, the "extinction distance" of the beam is even less. For a reflection diffraction experiment, where a monoenergetic beam must enter the crystal, and beams with the same energy must exit again, the mean "sampling depth" is half the value of the extinction distance.

For high-energy electrons or x-rays, the mean free path is much larger. However, as Eq. (12) shows, the limited penetration necessary for surface sensitivity can be achieved by making  $\theta_0$  and  $\theta$  large, i.e. by

grazing incidence and exit. Eq. (11) therefore also gives the interference function for RHEED and grazing-angle x-ray diffraction. One can again think of this reciprocal lattice in terms of the approximation of rods.

### B. Surface Defects

So far it has been assumed that the crystal surface is infinite, perfect, and rigid. In this case, the reciprocal-lattice rods will have zero width and the diffraction spots will be sharp. In the presence of defects the reciprocal-lattice rods have a finite width. This can be readily seen by letting  $N_1$  or  $N_2$  be finite in Eq. (7), in which case the corresponding term is no longer a delta function, but rather a function of the form  $\sin^2 Nx/\sin^2 x$ , (where  $x = 1/2 \frac{S \cdot a}{a}$ ), which has a nearly Gaussian shape in its center, a full width at half-maximum (FWHM) proportional to  $1/N$ , and wings higher than those of a Gaussian profile, with  $(N-2)$  side bands that are distinct if  $N$  is small and unresolvable if  $N$  is large. Limitations in the order or the size of a crystal in the dimension parallel to the surface thus cause a different behavior than limitation of the crystal in the direction perpendicular to the surface caused by finite penetration. In the latter case subsidiary maxima do not occur because the amplitude from each plane is different. In the former, each row of atoms scatters the same amplitude, and therefore, if the finite-size effects are regular, distinct subsidiary maxima can be observed. In many cases, of course, the disorder is random (e.g. many small ordered regions of different sizes) and the subsidiary maxima wash out to leave only a broadened Bragg peak and a diffuse background.

#### B.1 Clean Surfaces

An example that illustrates generally the broadening of reciprocal-

lattice rods caused by defects can be given by considering a distorted crystal, where the position of the  $j$ 'th lattice site (or unit cell) is now

$$\underline{r}_j' = \underline{r}_j + \underline{R}_j, \quad (13)$$

where  $\underline{R}_j$  is the vector giving the displacement of the unit cell from its proper position  $\underline{r}_j$ . To describe this density function, more Fourier components are necessary than for a perfect crystal. Around a particular reflection  $\underline{G}_{hk1}$ , Eq. (4) becomes

$$A(\underline{G}_{hk1} + \underline{s}) = F(\theta, E) \int_j \exp [i (\underline{G}_{hk1} + \underline{s}) \cdot (\underline{r}_j + \underline{R}_j)]. \quad (14)$$

The presence of the imperfection thus introduces an added phase factor  $\exp [i (\underline{G}_{hk1} + \underline{s}) \cdot \underline{R}_j]$ . Consider  $\underline{R}_j$  to be a sinusoidal variation in spacing in the  $\underline{a}$  direction, i.e.,

$$\underline{R}_j = \underline{a} \cos \frac{2\pi x_j}{A}, \quad (15)$$

where  $\underline{a}$  is very small compared to  $\underline{a}$  and where  $A$  is the wavelength of the modulation. Then for the reflection  $\underline{G}_{hk1}$ ,

$$A(\underline{G}_{hk1} + \underline{s}) = F(\theta, E) \int_j \exp [i (\underline{G}_{hk1} + \underline{s}) \cdot \underline{r}_j] \exp [i (\underline{G}_{hk1} + \underline{s}) \cdot \underline{a} \cos \frac{2\pi x_j}{A}], \quad (16)$$

neglecting the term  $(\underline{s} \cdot \underline{R}_j)$ . Because  $\underline{a}$  is small, the second exponential can be expanded to give

$$A(\underline{G}_{hk1+s}) = F(\theta, \epsilon) \int \exp [i(\underline{G}_{hk1+s}) \cdot \underline{r}_j] \\ + i \underline{G}_{hk1} \cdot \underline{\delta} \cos \frac{2\pi x_j}{A} \exp [i(\underline{G}_{hk1+s}) \cdot \underline{r}_j] \cdot \quad (17)$$

The first term is just the Fourier transform of the perfect crystal, while the second leads to sidebands at positions  $s_x = \pm 2\pi / A$  away from the main peak. If the crystal has a dimension  $N_1 a$  in the  $\underline{a}$  direction the rods will be broadened, with a FWHM of the rods in the  $\underline{a}$  direction of  $\Delta s_x = 2\pi / N_1 a$ . If  $A \gg N_1 a$ , the sidebands merge with the main rod and cause further broadening that increases with increasing  $h$  because of the factor  $\underline{G}_{hk1} \cdot \underline{\delta}$ . If  $A \ll N_1 a$ , the extra intensity goes into a background and leaves the main rod unchanged in width but reduced in intensity.

The effect on the reciprocal lattice of several types of defects can be illustrated by considering their wavelength  $\lambda$ . For example, most of the Fourier components of displacements due to thermal vibrations have  $\lambda$  of the order of atomic dimensions, which is much smaller than the dimension of a typical ordered region on a crystal surface. Hence thermal vibrations cause a diffuse background intensity that reduces the intensity at the  $(hk)$  rod but causes no broadening. Similarly, point defects have Fourier components that have mostly small  $\lambda$ , and they thus produce only a diffuse background. Random lattice strain, on the other hand, can have a much longer wavelength, of the size of the crystal, i.e.,  $\lambda \approx N_1 a$ . Hence random strain causes broadening of reciprocal-lattice rods that increases with increasing  $\underline{G}_{\parallel}$ , the parallel component of a reciprocal lattice vector. The dependence of the broadening on  $\underline{G}_{\parallel}$  due to random lattice strain at the surface<sup>(48)</sup> is shown schematically in Fig. 5.

Other defects that are not as easily explained in the above context can also exist at a surface. For example, subgrain (mosaic) structure in a crystal, shown in Fig. 6a, manifests itself at the surface as finite-size domains that have small misorientations with respect to each other. Typical mosaic dimensions in well-grown crystals are of the order of 1  $\mu$ m or larger, and misorientations are of the order of a tenth to several tenths of a degree. This misorientation causes a broadening of all reflections with  $\underline{G}_{\parallel}$ , the normal component of a reciprocal-lattice vector, as is illustrated in Fig. 6b. The broadening is easily understood by recognizing that each crystallite has its own reciprocal lattice normal to its surface and that these must have a common origin. Misorientations of 0.1° are readily observable by making angular profile measurements at various energies (i.e.,  $\underline{G}_{\parallel}$ )<sup>(49,50)</sup>.

Surface steps represent an entirely different type of defect. Many arrangements of steps are possible on a surface, with distinctive effects on the reciprocal lattice. The step arrangement for which the reciprocal lattice is visualized most easily is a monotonically increasing or decreasing step array with constant terrace size. As shown in Fig. 7, the reciprocal lattice can be considered as the product of the terrace structure factor and the reciprocal lattice associated with the average surface. This is equivalent to saying that the surface is the convolution of the single terrace unit with the step "lattice". The lattice points for this lattice represent the repeat units for the average surface, i.e., there is one lattice point associated with each terrace. Because the average surface consists of many "lattice" points, the reciprocal-lattice rods corresponding to the average surface will be sharp. Because the lattice points are far apart, the reciprocal-lattice rods are close

together. Their separation is inversely related to the cosine of the angle of cut: the greater the deviation from singular, the farther apart these rods will be. The terrace structure factor is just the reciprocal lattice associated with a single terrace. Because the terrace has finite dimensions  $N_1a$  and  $N_2b$ , the reciprocal-lattice rods corresponding to a single terrace will be broad, as discussed earlier. The greater the deviation of the average surface from singular, the smaller will be the terrace size and hence the greater will be the broadening. It should be evident that as the distribution of intensity due to the terrace structure factor gets broader (i.e., smaller terraces), the reciprocal-lattice rods of the average surface get farther apart (i.e., the repeat unit for the average "lattice" gets smaller). The product of these two factors, analogous to Eq. (6), is observed in reciprocal space.

Other step distributions produce different reciprocal lattices<sup>(25)</sup>. For example, if the terrace size remains uniform, but the steps are alternately up and down, the reciprocal lattice consists of rods modulated in  $G_{\perp}$  that are not inclined, because the average surface is flat. This is illustrated in Fig. 8 and can be explained simply in the following manner. As shown in Fig. 8a, the periodicity of the step structure is  $2Na$ , where  $N$  is the effective number of scatterers in one terrace. The interference function can be described as the product of three structure factors, one that describes the periodicity with  $2Na$ , one that reflects the scattering from one terrace of dimension  $Na$ , and one that gives the interference between terrace and trough. The first,  $|F_1|^2$ , is a reciprocal lattice consisting of rods that are delta functions (because this structure is infinite) spaced  $2\pi/2Na$  apart, and oriented normal to the surface. The separation of adjacent rods, i.e.,  $n = 0$  and  $n = 1$ , reflects

the size of one terrace plus one trough.  $|F_2|^2$ , the structure factor of one terrace of dimension  $Na$ , consists of an intensity function of form  $\sin^2(N\underline{s} \cdot \underline{a}/2)/\sin^2(\underline{s} \cdot \underline{a}/2)$  with maxima spaced  $2\pi/a$  apart (because  $\underline{a}$  is the repeat unit in a terrace) and with  $N-2$  subsidiary maxima. The rods are again oriented normal to the surface. The main maxima have a FWHM of  $2\pi/Na$ , and overlap three of the delta-function rods. The minima of the terrace structure factor occur on alternate delta-function rods, as do the subsidiary maxima.  $|F_3|^2$  takes the difference in  $z$  spacing between terraces and troughs into account. This can easily be shown to be a function of the form  $|F_3|^2 \sim 2[1 + \cos(h\pi) \cos(\underline{G}_{\perp} d)]$ , where  $h = 0, 1, 2 \dots$  is the order of the reflection and  $d$  is the height difference between terraces and troughs. If this function is evaluated at different values of  $\underline{G}_{\perp}$ , it is found that its zeros occur alternately at the  $n = \text{even}$  and  $n = \text{odd}$  rods. The product of all three structure factors gives the reciprocal lattice shown in Fig. 8c, with the rods with  $n = 0, 2N \dots$  having maximum intensity, the adjacent ones having about half as much intensity, and the subsidiary rods having a few percent of the intensity of the main rods, depending on the size of a terrace. They are all, in principle, visible, although the subsidiary maxima may be quite weak.

The periodicity of the oscillation in  $G_{\perp}$  is quite evidently related to the step height, as can be seen from the third structure factor. Physically this can be interpreted as constructive and destructive interference between terraces and troughs. When the interference is constructive, the diffraction does not recognize the existence of steps and only the reflections corresponding to an infinite lattice with lattice constant  $\underline{a}$  appear, at  $2\pi h/a$ . At other  $\underline{G}_{\perp}$ 's, all the other rods appear, and at characteristic  $\underline{G}_{\perp}$ 's the rods at  $2\pi h/a$  disappear while all the

others are present. Each rod displays the same periodicity in  $G_{\perp}$ , but with minima displaced in  $G_{\perp}$  because the phase shift due to  $G_{\parallel}$  is proportional to  $h$ . This periodicity in  $G_{\perp}$  is reflected in all stepped structures that have a unique step height or multiples of such a unique height. Thus it is always possible in such cases to extract the step spacing, simply from the periodicity of the oscillation or modulation in width of the reciprocal-lattice rods.

Introducing a distribution of terrace sizes causes broadening of reflections rather than a set of sharp delta functions. The most general case, shown in Fig. 9, is for random up and down step edges occurring at random intervals.<sup>(25)</sup> This situation is approximated by most surfaces that are nominally flat but contain steps. The situation is similar to the alternate up and down terraces of uniform size, except that, because of the randomness, the original delta-function term,  $|F_1|^2$ , is absent and  $|F_2|^2$  does not have subsidiary maxima but only a diffuse monotonically changing intensity between the maxima. The reciprocal-lattice rods alternately broaden and narrow as  $G_{\perp}$  is changed. The periodicity of the broadening is again related easily to the step height. At the conditions for which all the terraces scatter in phase, the diffraction spots will be sharp. At other  $G_{\perp}$ 's, there will be partial destructive interference and the spots will broaden. They will be broadest (for step distributions that contain only monatomic steps or a predominance of them) half way between the sharp spots.

If there is a predominance of steps of a height different from monatomic, the broadening will be different.<sup>(26)</sup> This is simply illustrated by considering all the steps to be double height, causing the periodicity in  $G_{\perp}$  to halve. As the step height multiplicity increases,

the period of oscillation decreases. A superposition of steps with a range of multiple-step heights leads to a distribution in reciprocal space as shown in Fig. 10. The broadening becomes flat over most of the range of  $G_{\perp}$ , with very sharp minima in width occurring at the positions of constructive interference, which do not change. A physical analog of multiaatomic steps is slip planes emanating at a surface. Slip in crystals can result, for example, during cleavage, and may result in step heights of 20 to 500 lattice constants.

### 3.2 Overlayers

Most of the phenomena mentioned above for clean surfaces have analogs in adsorbed overlayers. The most commonly observed (if not the most common) form of adsorbed monolayer is one that is commensurate with the substrate (i.e., adsorbed in regular lattice sites of the substrate) and with a unit mesh larger than that of the substrate (i.e., with a superlattice). Such layers are identified with a standard notation indexed to the substrate unit mesh, such as  $W(110)p(2 \times 1)-0$ , which indicates an overlayer of 0 on the  $W(110)$  face that has a unit mesh dimension that is twice the substrate unit mesh dimension in the  $a$  direction and the same size as the substrate unit mesh in the  $b$  direction. "p" indicates that the overlayer unit mesh is primitive, i.e., it contains only one atom. Similarly  $W(100)c(2 \times 2)-H$  indicates an overlayer of H on the  $W(100)$  face that has unit mesh vectors twice that of the substrate in both  $a$  and  $b$  directions, but additionally includes an atom in the center of the mesh. It is thus not primitive. An equivalent notation for this overlayer that does give a primitive mesh is  $W(100)p(\sqrt{2} \times \sqrt{2})R45^\circ-H$ , where  $R45^\circ$  indicates that the overlayer unit mesh is rotated by  $45^\circ$  relative to that of the substrate. Overlayers with

a periodicity different from that of the substrate produce additional, or superlattice, reciprocal-lattice rods. The positions of these superlattice rods can be established by substitution of the proper superlattice unit mesh vectors for  $\underline{a}$  and  $\underline{b}$  into Eq. (7), or else by an argument similar to that given by Eq.'s (9)-(13), which will demonstrate that the new Fourier components produce a "sideband" at the proper reciprocal-lattice positions. The reciprocal lattice for a complete, infinite, perfectly ordered monolayer with a double periodicity in the  $\underline{a}$  direction [e.g.,  $p(2 \times 1)$ ,  $p(2 \times 2)$ ,  $c(2 \times 2)$ ] is shown in Fig. 11a. The intensity distribution consists of delta-function rods.

Another form of adsorbed layer is an "out-of-registry" layer, where the spacing of the overlayer atoms is slightly different from that of the substrate. If one considers an atom at an origin "lining up" with a substrate atom then the  $(N + 1)$ 'st overlayer atom will again line up, but with the  $N$ 'th substrate atom, leading to a superlattice with a large wavelength. The Fourier transform of this spacing gives sidebands, close to the main maximum, called satellite reciprocal-lattice rods. The formation of satellite lines can be caused by an overlayer that may be rotationally or translationally out of registry, by a periodic lattice distortion of the substrate caused by overlayer adsorption, or by similar effects.<sup>(51,52)</sup> If the distortion or displacement has a definite period, the satellite reflections will be sharp. Because the wavelength  $\Lambda$  of the distortion is generally large relative to a lattice constant, the satellite reflections will lie close to the position of the reflections for the undistorted or undisplaced lattice. There should be a multiplicity of sidebands, at values of  $s_x = \frac{2\pi n}{\Lambda}$ , with the one nearest the main peak being the most intense.

Any commensurately adsorbed monolayer that forms a superlattice will have translational and possibly also rotational (depending on the symmetry of the unit mesh) antiphase domains. A monolayer may exist in the form of two-dimensional antiphase islands<sup>(21,27)</sup> at some finite temperature if there is a net attractive interaction between the adsorbate atoms. There are a number of reasons why a submonolayer might exist as a distribution of islands, the most important being kinetic limitations and substrate point or line defects that act as nucleation sites. The reciprocal lattice appropriate for a submonolayer that forms antiphase islands depends on the coverage and on the type of antiphase boundaries that can exist for the structure. A reciprocal lattice that is generally applicable at low coverages for overlayers that form a superlattice is shown in Fig. 11b. A distribution of overlayer island sizes is assumed. The superlattice reciprocal-lattice rods broaden while the fundamental reflections consist of a broadened contribution, due to the overlayer islands, and a delta function resulting from the periodicity imposed by the substrate. This same reciprocal lattice results at any coverage for overlayer structures in which rotational antiphase domains are allowed [e.g.  $p(2 \times 1)$  and  $p(1 \times 2)$ ]. This is easy to understand. At low coverages, islands will be separated by a considerable amount of "sea". Because of the translational antiphase boundaries that always exist in overlayers with a superperiod, these widely separated ordered overlayer regions will be uncorrelated in phase (except at the precise Laue condition). The diffracted intensity from the overlayer consists of the sum of intensities from the individual islands.<sup>(21,27)</sup> There is interference, however, between the amplitudes scattered from the substrate and from the randomly arranged islands, making the relative strengths of the delta function and the scattering

from the overlayer dependent on diffraction conditions.<sup>(53)</sup> The reason that an overlayer with rotational antiphase domains acts in the same way, independent of coverage, is that these domains can't interfere with each other, and thus one always acts as "sea" for the other.

For an overlayer that forms only translational antiphase boundaries (e.g.  $p(2 \times 2)$ ) the reciprocal lattice is identical to that shown in Fig. 11b at low coverages. At saturation coverage there is no "sea", and because the fundamental reflections are not sensitive to antiphase boundaries that occur at integral multiples of the fundamental spacing, these rods will not have the diffuse wings, but will be sharp, as shown in Fig. 11c. The superlattice rods are broadened, because they are sensitive to antiphase boundaries.

If the overlayer adsorbs commensurately but without a superlattice [ $p(1 \times 1)$  structure], there obviously will be no superlattice reciprocal-lattice rods. If two-dimensional islands form, the reciprocal-lattice rods at low coverage will be identical to the fundamental reflections shown in Fig. 11b. For a  $p(1 \times 1)$  layer there can be no rotational antiphase domains, nor translational antiphase domains in the sense that we have so far described, i.e., occupation of the same type of sites but translationally displaced by a multiple of the substrate lattice constant. At saturation coverage the rods will therefore ordinarily be sharp, as shown in Fig. 11c for the fundamental reflections. However, a translational antiphase boundary of a different type can occur. This requires the occupation of two types of sites, e.g., hcp and fcc sites on an fcc (111) surface. The resulting antiphase boundaries (called twin or stacking-fault boundaries in bulk films or crystals) cause selective broadening of some of the reciprocal-lattice rods. Fig. 12 shows a

schematic diagram of an overlayer with a twin boundary and the resulting reciprocal lattice in one direction. The selective broadening of some rods can easily be understood physically by recognizing that the translational mistake at a twin boundary is less than one lattice constant, thus causing broadening of all those rods where the phase does not sum up to one, and no broadening where it does.

Finally, overlayers may form as completely incommensurate layers that, in a sense, form two-dimensional ordered rafts that have no definite phase relationship to the substrate on which they are adsorbed. The overlayer has its own reciprocal lattice. At any coverage below a monolayer, this system behaves like a two-dimensional mosaic, i.e., there is a random phase relationship between ordered islands, but, if the substrate is flat, there is no out-of-plane misorientation of the overlayer islands. If only translational randomness exists, (i.e., all the islands are oriented in the same manner) the reciprocal lattice is as shown in Fig. 13. The (00) rod is a delta function, because the specular reflection is not sensitive to lateral phase shifts. All the other rods will be uniformly broadened. Because completely incommensurate layers will generally also involve rotational randomness, the rods turn into rings of finite width, for all but the (00) rod.

Islands adsorbed on a substrate cause a modulation of the shape of the fundamental reflections with  $G_{\perp}$  for the same reasons that steps do, namely there occurs an interference between substrate and adsorbate layer. For self-adsorbed layers, which form  $p(1 \times 1)$  structures, this is obvious, because they are directly analogous to terraces. The same reciprocal-lattice rod shapes described for step structures are possible for such systems. For systems in which the overlayer atom is different



from the substrate atom a weak modulation of the shape of fundamental reflections should also exist, but it may no longer be simply oscillatory with the inverse of the layer spacing. Because the scattering factors are different for substrate and overlayer atoms, there may be a phase difference upon scattering from the overlayer and substrate. This phase adds to that due to the path difference and may shift the minima or distort the period of modulation.

In this section we have summarized basic elements of diffraction theory, in the kinematic limit. We have shown how surface-sensitive diffraction techniques can be discussed in terms of the Ewald construction and the relevant reciprocal lattice. A number of reciprocal lattices that correspond to various types of surface disorder have been presented. A perfect instrument has been assumed throughout this section. In the next section we take the opposite approach. We assume that the crystal is perfect but that the instrument, like all real instruments, has a finite sensitivity and a finite resolving power. We discuss the influence of these limitations on the measurement of diffracted intensities and on the accuracy of surface crystallographic determinations.

### III. The Measurement of Diffracted-Intensity Distributions

A diffraction experiment requires the creation of a beam of radiation to use as a probe, and the detection, at specific diffraction geometries, of the radiation scattered elastically by the sample. For accurate structural analysis, the intensities must be precisely measurable, and intensities scattered into different directions or at different energies must be distinguishable. The performance of a diffractometer in these respects can be described in terms of its

sensitivity and its resolving power. An instrument cannot be optimized in both; maximum sensitivity can only be achieved at the expense of resolution and vice versa.

#### A. Sensitivity

In a diffraction experiment one is, in essence, counting particles arriving in a particular direction, and therefore the best obtainable ratio of the intensity of the true signal to the noise current can be described by the well-known relationship between signal and shot noise,<sup>(54)</sup>

$$\frac{J_{\text{true}}}{J_{\text{shot noise}}} = \sigma (of t)^{1/2}, \quad (18)$$

where  $i$  is the incident-beam current,  $t$  is the time of measurement, and  $\sigma$  is the probability of measuring a diffracted particle for each incident particle.  $\sigma$  can therefore be identified with the sensitivity in a measurement. It includes both physical factors, such as scattering and the inelastic-scattering cross section, and instrumental factors, such as detector size and sensitivity. It is clear from Eq. (18) that the simplest way to increase the signal-to-shot-noise ratio is to increase the dose, i.e., to raise the incident current  $i$  or measure for a longer time  $t$ . In surface diffraction experiments it is frequently not possible to increase  $i$  arbitrarily because structural or chemical changes are introduced as a result of surface heating. It is also not possible to measure for arbitrarily long times, because the surface becomes contaminated. Surface contamination can, in fact, be considered the  $1/f$  or flicker noise in the measurement. In addition, electron beam damage is dose-dependent, and many surfaces and overlayers are quite sensitive to electron beams in the applicable energy ranges.

In LEED and RHEED, low sensitivity manifests itself in the inability to measure the intensity of small peaks accurately and reproducibly or to obtain an intensity map with sufficient data for reliable structural analysis in the time available before the surface structure begins to change. The magnitude of the background intensity is also significant, because the shot noise is proportional to the sum of the true and background intensities. A large background can therefore significantly degrade the reliability of intensity data.

The most effective approach to improving the signal quality is to increase the sensitivity of the instrument. This will be addressed briefly later.

#### B. Resolving Power

Instrumental factors also limit the resolving power of the instrument, i.e., they cause a loss in attainable accuracy in measuring the shapes of reciprocal-lattice rods. It is possible to quantify this contribution.<sup>(55)</sup> If  $T(\vartheta, E)$  represents the broadening, or instrument response, function,<sup>(56)</sup> the measured intensity is given by the convolution.

$$J(\vartheta, E) = I(\vartheta, E) * T(\vartheta, E), \quad (19)$$

or equivalently

$$J(S) = I(S) * T(S). \quad (20)$$

$I(\vartheta, E) \propto I(S)$ , the true signal, results from the incoherent sum of diffraction patterns of individual electrons all with the same momentum.

$I(\vartheta, E)$  is a delta-function if the surface is perfect and is a function with some angular spread or "physical width" if the surface is not perfect.  $T(\vartheta, E)$  can be thought of as a shape function, whose integral is unity, that distributes the true intensity  $I(\vartheta, E)$  over a range of angles

and energies in reciprocal space. The major sources of instrumental broadening in diffractometers are the incident-beam divergence or "source extension",  $\gamma$ , of the electron gun; the energy uncertainty in the incident beam,  $\Delta E$ ; the incident-beam diameter,  $D$ ; and the detector aperture width,  $d$ . As discussed by Park et al.,<sup>(56)</sup> the instrument response function, the distribution in momentum of all the electrons arriving at the detector if the sample is perfectly periodic, will be

$$T(\vartheta, E) = T(\vartheta, E)_{\gamma} * T(\vartheta, E)_{\Delta E} * T(\vartheta, E)_{D} * T(\vartheta, E)_{d}. \quad (21)$$

The total instrument response measured for a typical commercially available LEED instrument has a Gaussian profile near its center, with wings that are more Lorentzian. Response functions have to our knowledge not been measured accurately for RHEED, grazing-angle x-ray diffraction, or atomic-beam scattering systems.

The different uncertainties that make up  $T(\vartheta, E)$  influence the accurate determination of the reciprocal lattice in different ways, some causing inaccuracies in  $G_{\parallel}$ , others in  $G_{\perp}$ , but most in both. It is instructive to consider the contributions to  $T(\vartheta, E)$  separately using the reciprocal lattice of a two-dimensional perfect crystal. Figure 14 illustrates some of these contributions, in both real and reciprocal space. Consider first an uncertainty in the energy of the incident beam. In order to isolate just this one uncertainty, assume an infinitely narrow parallel beam, i.e., two coaxial rays, with slightly different  $|k_{\parallel 0}|$  vectors, falling onto an infinite, perfectly periodic two-dimensional crystal. The reciprocal lattice and diffraction geometry for the (00) reflection are shown in Fig. 14a. Because the wave vectors  $k$  must all end

on a rod, it is clear that an averaging in  $G_{\perp}$  results, i.e., all values of intensity along the rod between the extremal value of the  $\underline{k}$  vectors are sampled. No broadening of the specular  $[(00)]$  beam results from an energy uncertainty in the incident beam because the  $\underline{k}$  vectors are all parallel. Thus for an infinite, perfect, two-dimensional crystal, if only an energy uncertainty exists in the incident beam, the  $(00)$  diffraction peak will be a delta function in angle whose intensity is some integral of the intensity along the rod over the range in  $G_{\perp}$  that is sampled.

For nonspecular beams, an energy uncertainty in the incident beam causes uncertainty in  $G_{\parallel}$  as well as an integration over a range in  $G_{\perp}$ , as shown in Fig. 14b. The  $\underline{k}$  vectors must still fall onto the rod, giving the average in  $G_{\perp}$ , but in order to do so, they emanate from the crystal at various angles of incidence. For an infinitely narrow, parallel incident beam, this would produce a diffracted beam that has a finite width at the detector. As indicated below, such a finite width represents an inability to determine precisely the value of  $G_{\parallel}$ , because it will give a reflection broadened in angle. Thus for nonspecular reflections, an energy uncertainty gives a measured profile that is some sample over  $G_{\perp}$  in which, as well, the value of  $G_{\parallel}$  is imprecise.

A similar situation obtains if there is an angular divergence in the incident beam. It is, however, somewhat more complicated to visualize. The condition of minimum influence of angular divergence occurs if the beam is focussed such that the particular diffracted beam that is being measured has minimum size at the detector. Even the best focussing effort will result in a beam that has a finite size and finite divergence at the detector. Finite beam size and finite divergence can be treated separately by considering each point in the beam area to be the focal

point for rays. Then the complete beam can be described by the convolution, as in Eq. (21), of the divergence contribution and the finite-beam-size contribution. Thus for the purposes of describing the influence of the beam divergence assume that it is possible to focus perfectly, i.e., to make an infinitely narrow beam at the detector that does, however, have some divergence. The corresponding real- and reciprocal-space diagrams for the  $(00)$  rod are shown in Fig. 14c. As for an energy uncertainty, an integration over a range in  $G_{\perp}$  results. The  $\underline{k}$  vectors are also not parallel. However, if it is assumed that this beam is focussed at the detector, there is no broadening in  $G_{\parallel}$  due to the beam divergence.

If the focussing conditions are set to focus the  $(00)$  beam on the detector, none of the other diffracted beams will be in focus. This can be seen from simple geometry by recognizing that the other reflections come from "mirrors" oriented differently with respect to the incident beam. Thus for any beam other than the one that is chosen for best focus, beam divergence will lead also to an uncertainty in  $G_{\parallel}$ , as shown in Fig. 14d. If the incident beam is focussed on the sample, all diffracted beams will be broadened in angle.

The important quantity in considering the contribution of finite beam width to the resolving power is the beam width at the detector. After removing the divergence the finite-beam-width contribution can be considered separately as resulting from a parallel beam that has a size given by the size of the beam at the detector. Each ray in this beam will be incident at the origin of reciprocal space, hence no averaging over  $G_{\perp}$  results from finite beam diameter. Uncertainty in  $G_{\parallel}$  results because a finite beam diameter translates into an angular uncertainty.

The angular width differs for different beams, as shown in Fig. 14e. It will be most severe for beams near normal exit. A lens before the detector may be used to focus a parallel beam to reduce the effect of beam diameter if the beam is itself parallel.<sup>(56)</sup>

The effect of finite detector aperture size is the same as that of finite beam diameter, i.e., it causes a broadening in  $G_{\parallel}$  because of the angle subtended by the detector at the sample. Unlike that of the finite beam diameter, the angular width of the finite detector aperture is not dependent on exit angle of the beam, as shown in Fig. 14f.

Several of these contributions influence the resolving power differently in different directions, causing asymmetric-spot-shape effects. To illustrate this, consider again the energy uncertainty in the incident beam. For the (00) beam, it causes integration only in  $G_{\perp}$ . For nonspecular reflections uncertainty in  $G_{\parallel}$  also results, but for some configurations, e.g., when  $k_0$  and  $k$  are coplanar, broadening occurs in only one direction in  $G_{\parallel}$ . This can be readily visualized with the help of the reciprocal-lattice constructions in Fig. 14.

The above discussion has illustrated the various contributions to  $I(\vartheta, E)$  and their effect on a measurement. It is evident that the instrument response differs at different diffraction conditions. The resolving power of an instrument at any diffraction condition can be quantified by defining a minimum angle of resolution. If one represents the instrument function  $I(\vartheta, E)$  by a Gaussian with a full width at half-maximum,  $b_T$ , and the accuracy to which this width is known and to which a measurement  $J(\vartheta, E)$  has been made as  $\Delta X$ , then the smallest value of the width of a signal  $I(\vartheta, E)$  that can be resolved by the instrument is<sup>(55)</sup>

$$\vartheta_{\min} = [(b_T + \Delta X b_T)^2 - (b_T - \Delta X b_T)^2]^{1/2} = 2b_T (\Delta X)^{1/2}. \quad (22)$$

Equation (22) represents the worst possible case for the resolving power of a given instrument, because it is based on extremal values of signal allowed by the error bars. The uncertainty in the measurement,  $\Delta X$ , is clearly related to the system sensitivity, and thus is a function of the incident beam current, the detector efficiency, and the measurement time. Methods to increase the resolving power by improving electron gun characteristics to give a better instrument response and by improving detector efficiency to give greater sensitivity are briefly addressed in a later section.

It has been mentioned earlier that different diffraction techniques observe the reciprocal lattice in different ways. The limiting cases are those appropriate for LEED and for RHEED. In the former, the incident beam is generally nearly normal to the surface, and the most frequently observed diffracted beams are those that emanate nearly normal to the surface. In the latter, the incident beam is very near grazing incidence (fractions of one degree to several degrees), and the diffracted beams likewise exit near grazing angles. The two techniques therefore give quite different cuts through the reciprocal lattice, with a consequently significant influence on the resolving power. In LEED, the beams emanating near backward directions represent cuts nearly perpendicular to a reciprocal-lattice rod. For a cut that is strictly perpendicular to the rod, no averaging in  $G_{\perp}$  results except that introduced by the instrument response,  $I(\vartheta, E)$ . Any other cut through a rod always gives an integral over  $G_{\perp}$  in addition to that introduced by  $I(\vartheta, E)$ . This is an important disadvantage in many experiments, especially on surfaces with defects, as

discussed in the next section, where several of the ways of measuring diffraction spots are more fully explored. Cuts not perpendicular to a rod also have an important positive consequence, however, in that they increase the resolving power in the plane of the cut.<sup>(57)</sup> This can easily be seen by considering a rod with finite width  $\Delta G_{\parallel}$ . A cut normal to the rod will give an angular width

$$\Delta \vartheta = \frac{\Delta G_{\parallel}}{k} \quad (23)$$

The intensity function with this width, is, of course, convoluted with the instrument function. Whether it is resolvable depends on the minimum angle of resolution,  $\vartheta_{\min}$ . A cut at an angle  $\vartheta$  will give an angular width

$$\Delta \vartheta = \frac{\Delta G_{\parallel}}{k \cos \vartheta} \quad (24)$$

where  $\vartheta$  is the angle the exiting beam makes with the surface normal. Thus as  $\vartheta$  increases,  $\Delta \vartheta$  increases until, at an exit angle of  $1^\circ$ , the angular width measured (in the plane of  $\underline{k}$  and the surface normal) for a rod of a given width  $\Delta G_{\parallel}$  is about 50 times that near normal exit. As the minimum angle of resolution is not significantly affected by exit angle (because of the dominance of the beam-size contribution to the instrument response in typical systems<sup>(58)</sup>), it becomes possible to distinguish much smaller  $\Delta G_{\parallel}$ , and hence the resolving power increases. A cut at  $45^\circ$  at LEED energies increases the angular width of a reflection by 1.4; a cut at  $70^\circ$  increases it by a factor of 3. In RHEED, the length of the  $\underline{k}$  vector

is greater, negating to some degree the effect of the small angle. Nevertheless, for a  $1^\circ$  exit angle and a 10 keV beam, the angular width ("streak length") of a reflection should be about seven times that observed for LEED at 150 eV and normal exit, and hence the resolving power is more than seven times as great in the plane defined by  $\underline{k}$  and the surface normal. In the plane perpendicular to this one the resolving power is, in fact, smaller than that of LEED by the ratio of the lengths of the  $\underline{k}$  vectors.

The resolving power of the instrument is meaningful only in terms of the real-space distances that can be resolved. Some simple examples will illustrate that for a given instrument, the resolving power depends on the type of defect that is present on the surface. We assume an instrument with a minimum angle of resolution  $\vartheta_{\min} = 0.5^\circ$ , typical for a conventional LEED system at 50 eV. We consider three cases:<sup>(55)</sup>

(1) Mosaic structure with translationally random phases only

In this model the surface is flat, but has domains of mosaic structure that are separated by random phases in a direction parallel to the surface. An example might be a saturation-coverage incommensurate overlayer consisting of many domains that have random translational phase relationships. Within each domain, the structure is assumed perfectly periodic with a lattice constant  $a$ . For simplicity, all domains are assumed to have the same size,  $N_1 a$ . The interference function is given by Eq. (7),

$$\tilde{I}(\underline{G}_{hk1} + \underline{s}) = N \frac{\sin^2 \frac{1}{2} N_1 (\underline{G}_{hk1} + \underline{s}) \cdot \underline{a}}{\sin^2 \frac{1}{2} (\underline{G}_{hk1} + \underline{s}) \cdot \underline{a}} \quad (25)$$

where  $N_1$  is the total number of atoms in each domain, and  $M$  is the number of domains within the diameter of the incident beam. For a normally incident beam, the FWHM,  $b_1$ , of the intensity function is related to the domain size by

$$b_1 = 0.888\lambda / (N_1 a) (a^2 - h^2 \lambda^2)^{1/2}, \quad (26)$$

where  $\lambda$  is the wavelength of the electron and  $h$  is the order of the diffracted beam from a set of surface rows, i.e. (00), (10), (20), etc.. For the first-order ( $h = 1$ ) diffraction maximum for diffraction from a surface with a lattice constant  $|a| = 3 \text{ \AA}$  the maximum size of flat mosaic domain that the instrument can resolve is

$$(N_1 a)_{\max} = 0.888\lambda / \theta_{\min} (a^2 - \lambda^2)^{1/2} \approx 215 \text{ \AA} \quad (27)$$

If  $\theta_{\min}$  is improved to  $0.2^\circ$ , either by increasing the accuracy of the measurement or by improving the instrument response, the maximum domain size that can be resolved is  $(N_1 a)_{\max} \approx 535 \text{ \AA}$ .

As can be seen from Eq. (27), the maximum observable domain size depends on the energy of the incident beam, the order of the diffracted beam (hence the incident and exit angles), the lattice constant, and the minimum angle of resolution.

(2) Flat continuous surface layer with translational antiphase boundaries and equal-size domains.

If the surface consists of a continuous phase containing translational antiphase boundaries, instead of a continuous phase with random phase boundaries as in Model 1, a definite phase relationship

exists between the domains. This is the approximate situation for many commensurate overlayers with high-symmetry superlattice structures [e.g.  $p(2 \times 2)$ ] at their saturation coverage. If there are a roughly equal number of each type of antiphase domain, all of size  $N_1 a$ , the superlattice Bragg reflections will be split into two peaks separated by an angle<sup>(55)</sup>

$$b_1 = \lambda a / N_1 a (a^2 - h^2 \lambda^2)^{1/2} \quad (28)$$

where the angular separation  $b_1$  reflects the periodicity introduced by the repetition of antiphase boundaries at regular intervals given by  $N_1 a$ , the domain size. The minimum angle of resolution is then interpreted as the smallest angular separation of the two spots that the instrument can resolve. For  $\theta_{\min} = 0.5^\circ$ ,  $E = 50 \text{ eV}$ ,  $a = 3 \text{ \AA}$ , and  $h = 1$ , the largest antiphase domain of this type that the instrument can resolve is

$$(N_1 a)_{\max} = \lambda a / \theta_{\min} (a^2 - \lambda^2)^{1/2} \approx 240 \text{ \AA} \quad (29)$$

(3) Flat continuous surface layer with translational antiphase boundaries and random-size domains.

If the domains in Model 2 are not the same size, but have a random distribution of sizes, with only translational antiphase boundaries between them, then instead of splitting, the superlattice Bragg reflections will be broadened. The FWHM  $b_1$  is related to the average domain size,  $\langle N_1 a \rangle$ , by<sup>(55)</sup>

$$b_1 = \frac{\lambda}{\langle N_1 a \rangle (a^2 - h^2 \lambda^2)^{1/2}} \cos^{-1} \alpha, \quad (30)$$

where

$$a = (4f - f^2 - 1)/2f \quad \text{and} \quad f = 1 - 2a/\langle N_1 a \rangle.$$

Again for  $\theta_{\min} = 0.5^\circ$ ,  $E = 50$  eV,  $a = 3$  Å, and  $h = 1$  the maximum average domain size that the instrument can resolve is  $(N_1 a)_{\max} \approx 155$  Å.

It is evident from this discussion that for a given instrumental response the resolving power differs for different types of defects that limit the order on a surface or in an overlayer. In addition, the resolving power may be different in different directions and for different techniques. Similarly the sensitivity may differ for different techniques and different instruments. Some diffraction measurements require high sensitivity, others high resolving power. In the next two sections we discuss the major types of diffraction measurements and the optimization of diffractometers in terms of sensitivity and resolving power.

#### IV. Surface Crystallography Measurements

In this section, the major types of surface crystallography measurements are described and the limitation of these measurements explored with reference to the last section.

##### A. Diffraction Patterns

The most common diffraction measurement is, of course, the observation of the diffraction pattern. From it the size and shape of the surface unit mesh and the existence of any superlattice can be obtained by inspection. Simply the presence or absence of reflections, their position, and their behavior with incident-beam energy can be used in investigations of the overlayer symmetry, the nature of the defects present, and the existence of possible phase transformations in an overlayer. Fig. 15a illustrates the corresponding LEED geometry in real and in reciprocal space. Fig. 16a illustrates the equivalent RHEED geometry. Generally the sensitivity of the diffractometer is of greater concern than the resolving power in overall visual observations, particularly in the search for "weak" diffraction features that may indicate the presence of an overlayer phase.

##### B. Equilibrium Position Determinations

Much of the activity in LEED has been in the determination of the equilibrium position of surface or overlayer atoms. Other surface-sensitive diffraction techniques have, on the other hand, essentially not been used in this way. Although the required data may be obtained in a variety of ways, the most common form is a measurement of the integrated intensity-vs-energy profile (commonly called an "I vs E" curve but more properly identified as a  $\int_{\text{detector}} J_{hk}(\theta, E) d\omega$  vs E curve). In this measurement, the intensity in a particular reflection  $J_{hk}(\theta, E)$ .

integrated over the solid angle of the detector,  $d\Omega = d\theta d\phi$ , is determined as a function of incident-beam energy, effectively scanning the reciprocal lattice in  $G_{\perp}$  at fixed  $G_{\parallel}$ . This is illustrated for LEED in real and reciprocal space in Fig. 16b. The sensitivity of the diffractometer is of primary importance in this measurement. Frequently this is simply because some peaks in the diffracted intensity (e.g., from fractional monolayers) are small. In other cases electron beam damage to the overlayer or surface structure requires use of as low a total dose as possible. Frequently, however, the need for sensitivity implies simply a need for speed in data acquisition, because a large data base is required for accurate analysis of the equilibrium positions, and because the LEED intensity is usually quite sensitive to surface contamination.

The integrated-intensity-vs-energy measurement represents a determination of the interference among the several layers that are illuminated by the incident beam (see Fig. 3). Because an integral is usually taken over the width of a particular reflection,  $\Delta G_{\parallel} = k \cos \theta \Delta \theta$ , finite-size effects are not resolved and generally will not affect the equilibrium-position determination. This need not be true in all cases, however.<sup>(59)</sup> The possible influence of finite-size effects on "intensity-vs-energy" profiles can be illustrated with Fig. 17, which shows a LEED measurement at various energies for a surface that contains random steps. An integrated-intensity measurement is obtained by using a detector (Faraday cup or telephotometer/screen) with a fixed aperture size chosen to be "large enough to collect the whole diffracted beam". This means in practice that the detector is approximately the size of the full width at half-maximum of the beam at some energy and the measurement is  $\int_{\text{detector}} J_{hk}(\theta, E) d\Omega$  vs  $E$ . However, a fixed-aperture

detector, because it subtends a constant solid angle at the crystal, collects an increasingly large fraction of the intensity in the Brillouin zone (including thermal diffuse scattering intensity) as the energy is increased. The effect is in all cases a more or less monotonically increasing background in "I vs E" curves, which causes a worse signal-to-noise ratio and a consequently larger uncertainty for high-energy peaks. Additionally, for a surface containing randomly distributed steps, the intensity distribution oscillates in width along the reciprocal-lattice rods, (Fig. 9) and as a result, as Fig. 17 illustrates, the fraction of the Bragg intensity that is collected can vary rapidly even within a few eV. This phenomenon can distort peak shapes or shift peaks in integrated-intensity-vs.-energy measurements.

Although a high resolving power is not a priori necessary for integrated-intensity measurements, the instrument response function must at least be well known in order to extract reliable data. This can be illustrated as follows. Because LEED instruments in different laboratories commonly have different beam parameters and detector widths, and because intensity-vs-energy data are usually collected with the detector centered on the maximum intensity rather than by scanning through the reflection, the measured "integrated" intensity  $\int_{\text{detector}} J_{hk}(\theta, E) d\Omega$  can differ markedly for the same  $I_{hk}(\theta, E)$  (i.e., for surfaces with identical structures and degree of order). Thus, for reliable equilibrium position determinations, a knowledge of  $I(\theta, E)$  is a necessity to allow an accurate evaluation of what the measured intensity represents.<sup>(59)</sup>

Intensity-vs-energy measurements are much more difficult with RHEED because it is not possible to obtain the intensity integrated over  $\Delta G_{\parallel}$



at any point  $G_{\perp}$  on a rod. Any finite-size effect gives a broadened rod. Because the Ewald sphere cuts rods at a grazing angle in RHEED, a streak results. In principle, it is possible to use a very small detector to obtain the intensity along this streak to get an intensity-vs-energy profile. This measurement, is however, complicated by instrument response (leading to some integration in  $G_{\perp}$  at every point in the measurement) and by the distribution of intensity in  $G_{\parallel}$  on the cut across the rod that is made by the Ewald sphere. Hence such measurements may not reflect very reliably the integrated intensity as a function of  $G_{\perp}$ .

It is customary in LEED to calculate directly the intensity distribution expected from a given model structure and to compare this with the measured intensity. A number of calculations for different structures are required to search for the most probable structure. In x-ray diffraction, where the interaction of the radiation with the material is weak, a single-scattering or kinematic calculation of the diffracted intensity is usually sufficient for structural analysis. Because of the strong interaction of electrons with the material, there are usually strong multiple-scattering events in LEED and RHEED. The energy positions of intensity maxima in a diffracted beam depend on the relative phases of the electron waves diffracted from the atoms in the surface, and thus depend both on the positions of the atoms and the phase shifts upon scattering from the atoms. The intensities are influenced by a number of effects, including thermal vibrations, structural order, energy loss mechanisms, and experimental factors. Dynamic LEED theories, which include the multiple scattering, have been developed and used for most surface structure determinations.<sup>(13-17)</sup> Because of the sensitivity of the energy positions of peaks in "I vs E" curves to geometric positions of

atoms, the structural analysis emphasizes a fit between peak positions in calculations and experiments. For simple structural problems (relaxation of the outer layer of a clean metal, overlayers with small unit mesh) visual comparison has been used successfully for structure determination, because the eye acts as an excellent discriminator and/or noise filter. For comparisons of large amounts of data, as is required with larger unit meshes, this becomes cumbersome. As a result, automated criteria, called reliability or R-factors, have been developed.<sup>(60)</sup> R-factors are single numbers summarizing the level of agreement between sets of curves, a small R-factor indicating better agreement. In order to be useful in discriminating one structural model from another, R-factors should be sensitive to surface atom equilibrium positions but insensitive to nonstructural parameters such as the scattering potential or even to other structural parameters such as surface defects or thermal disorder. Unfortunately, because an R-factor can be sensitive to any of a number of features in a "I vs E" curve, e.g., peak positions, slopes, relative peak heights, small peaks, large peaks, etc., it is difficult to design one that objectively measures the best fit between theory and experiment. Attempts to develop a globally sensitive R-factor have so far failed.<sup>(60)</sup> No single R-factor presently in use is totally satisfactory for reliable structure analysis. The best structure analysis results from an average of all R-factors. The spread in R-factor values for any structure may be significant for structure determination: the smaller this spread, the more likely the structure is correct, independent of the absolute values of the R-factors.<sup>(60)</sup>

The existence of multiple scattering in principle makes electron diffraction very sensitive to small structural differences.

Unfortunately, the resulting theoretical problem also becomes quickly unmanageable in terms of the computing time needed to perform a range of structural searches. One approach that alleviates this difficulty is to limit the required range of search by extracting the single-scattering intensity in "I vs E" curves and using it to provide likely bounds to some of the structural parameters. Because it depends only on the momentum transfer vector  $\underline{S}$  and not on  $\underline{k}_0$  and  $\underline{k}$ , the single-scattering intensity can be determined by making a number of measurements at constant momentum transfer,  $\underline{S}$ , and averaging them.<sup>(61,62)</sup> The single-scattering intensity can then be interpreted with simple modifications of methods that were developed for x-ray diffraction to provide approximate values of surface or overlayer atom structural parameters. Two ways of making "I vs E" measurements that keep  $\underline{S}$  fixed but change  $\underline{k}$  and  $\underline{k}_0$  so that the multiple scattering changes are shown in Fig. 18.

### C. Structural Defects

A major and increasingly popular application of surface-sensitive diffraction techniques is in the determination of surface defects. The required measurement is the angular distribution of intensity in individual diffracted beams  $\int_{\Omega} J_{hk}(\vartheta, E) d\Omega$  vs  $\vartheta$ . When this measurement is made at various diffraction conditions (e.g., energy, angle of incidence, various diffracted beams), different surface defects can be identified because of their differing, but characteristic, influence on the beam profile. The precision of such measurements depends on the resolving power of the diffractometer, as already indicated. This implies a need for highly accurate measurements and good electron beam characteristics, including low divergence and energy spread and a small beam size, as well as a small detector aperture. Although much work has recently been done on increasing both sensitivity and resolution, especially in LEED diffractometers, very high resolution can be obtained only at the expense of sensitivity. Thus most high-resolution surface defect studies are so far made on static defect distributions on surfaces stable against beam damage or rapid contamination, where sufficient time is available to signal average the intensities.

Angular-profile measurements can be made in a number of different ways. These are shown schematically in real and reciprocal space in Figs. 15 c, d, and e, and in Fig. 16b. In the most commonly used LEED method, shown in Fig. 15c, the detector is scanned through a diffracted beam. In the second method (Fig. 15d) the detector is fixed and the crystal is rocked so that the desired reflection moves across the detector. There are two advantages of this method. The cut across a rod is flatter than if the detector is moved, because it has a radius of  $|\underline{S}|$

rather than  $\frac{h}{m\lambda}$  and, because the triangle  $k_0$ ,  $k$ ,  $S$  stays fixed, the scattering angle  $2\theta$  is constant. As a result, there are no variations in the scattering factor  $f(\theta, E)$  across a profile with this method.<sup>(63)</sup> Asymmetries in angular profiles caused by a changing  $f(\theta, E)$  can be significant over the width of a Brillouin zone, especially at low energies where  $f(\theta, E)$  can vary rapidly with angle and where the width of a zone represents a large angular change (i.e., the diffracted-beam separation is large at low energies). The disadvantage is that a mechanical motion, i.e., tilting the sample, is required. This generally cannot be done as accurately as scanning the detector, especially if electronic detection is used. In addition, the angle of incidence changes, introducing possible multiple-scattering effects involving other diffracted beams. The third method for angular profile measurement, (Fig. 15e), advanced originally for LEED intensity-vs-energy profile measurements<sup>(6,18)</sup>, consists of scanning the energy of the incident beam sufficiently so that the diffracted beam moves across a fixed detector. The cut across the rod is elongated for diffracted beams near normal incidence, which, as has been discussed, can be both an advantage and a disadvantage. The advantage is high resolving power in the plane containing the surface normal and the diffracted beam. The disadvantage is the large range of  $G_{\perp}$  that is included, causing an uncertain interpretation of the beam shape if the rod itself has structure. A second disadvantage is the possible introduction of multiple-scattering effects that are dependent on energy. An advantage is that no mechanical motion is required.

There are a number of inherent difficulties in making LEED angular-profile measurements with high precision. The most important of these

is suppression of inelastically scattered electrons, including the "quasielastic" thermal diffuse scattering. The angular distribution of these electrons will in general differ from that of the elastically scattered ones, and will therefore distort a measurement of the latter, especially in the wings of the angular profile, which are the most sensitive to the defect density and defect distribution. It is not a simple task to remove inelastically scattered electrons while at the same time not disturbing the angular distribution of the elastically scattered ones. The usual method of suppression of inelastically scattered electrons is with a high-pass filter consisting of a retarding-potential grid in front of the detector. It has been shown<sup>(9)</sup> that, in order not to disturb measurably the angular distribution of the diffracted electrons passing through a typical LEED grid structure, the retarding bias on the grid can be no more than about 80-90% of the energy of the diffracted beam. This implies that all those inelastically scattered electrons that have energies within 10-20% of the elastically scattered electrons will contribute to the measured profile. In order to remove this contribution, it is necessary to know the angular distribution of those inelastically scattered electrons that pass through the grids. It is usually assumed to be a constant, in which case a constant background can be subtracted from the angular profile. Alternate methods for measuring the elastically scattered electrons while suppressing the inelastically scattered electrons involve the use of magnetic fields or special geometries of a Faraday cup.<sup>(46)</sup> The most accurate measurement of the elastically scattered electron current accurate can be made with an electron energy analyzer in front of a Faraday cup collector. Detectors will be discussed in a

later section.

Although a major fraction of the inelastically scattered electrons can always be removed without noticeably affecting the angular profile, the remaining inelastic-scattering intensity can cause significant noise in the wings of the profile. Statistical noise goes up as the square root of the signal plus background; thus even after background subtraction, the elastically scattered intensity may have large uncertainties.

An even more serious problem is the thermal diffuse or phonon scattering.<sup>(63-65)</sup> Because the energy losses (or gains) associated with phonons are only at the order of tens of meV, they are too small to be resolved with the energy resolution typically achievable at the energies of LEED or RHEED experiments.<sup>(66)</sup> Thus phonon scattering is present to some degree in all angular profiles of diffracted intensity. The magnitude of the phonon contribution to the total intensity can be roughly estimated from a knowledge of the Debye temperature of the surface under investigation or from a measurement of the Debye-Waller factor of this surface. The Debye-Waller factor, obtained by measuring the decay of the Bragg peak intensity with increasing temperature at any energy,

$$J(\underline{s}, T_2) = J(\underline{s}, T_1) \exp(-2M) \quad (31)$$

gives the value of

$$2M = \langle \underline{s} \cdot \underline{u} \rangle^2 = 4\pi (\sin^2 \theta) \hbar^2 T / \lambda^2 m k_B \Theta_D^2, \quad (32)$$

where  $\langle u^2 \rangle$  is the mean square vibrational amplitude of surface and near-surface atoms,  $\theta$  the scattering angle,  $\lambda$  the wavelength of the radiation,  $T$  the temperature,  $m$  the mass of the surface atoms,  $k_B$  Boltzmann's constant, and  $\Theta_D$  the effective surface Debye temperature of the material. Most materials have a value of  $2M$  of the order of 2 or 3 at room temperature and 100 eV incident-beam energy. Figure 19 shows a plot of the dependence of the thermal-diffuse-scattering intensity integrated over a Brillouin zone on  $2M$ . The phonon scattering can be considered to consist of one-phonon and multiphonon contributions. The multiphonon scattering is uniformly distributed<sup>(64,65)</sup> over the Brillouin zone, while the one-phonon scattering is peaked near the diffraction maximum and falls off roughly as  $1/|s_{\parallel}|$ , where  $|s_{\parallel}|$  is the deviation parameter (see Eq. (6)) parallel to the crystal surface.<sup>(64)</sup> The multiphonon scattering can thus be removed by subtracting a constant background. The one-phonon scattering must be modeled<sup>(67)</sup> on the basis of the value of  $2M$  and the resulting integrated intensities from Fig. 19.

The simplest and most reassuring experiment that serves at least approximately to estimate the phonon scattering is to compare measurements of angular profiles of a high-quality surface taken at low and at high temperatures. If no differences are observed in the two profiles, the phonon scattering is not a significant factor in the angular distribution, to the accuracy that it is measured. The phonon scattering can be reduced by proper choice of the diffraction parameters (i.e. measurements at low momentum transfer). With the assumption that the phonon scattering does not depend significantly on surface or overlayer order or defect density, the profile measured on the high-

quality surface will serve as an instrument response function that also accounts for the thermal diffuse scattering contribution to the angular profile taken on the surface containing defects.

Angular profile measurements in RHEED are illustrated in Fig. 16b. These could be made with a moveable detector or by scanning the patterns with a vidicon. Experimental considerations (discussed below) make it practical to deflect the beam across a fixed detector, however.<sup>(68)</sup> Intensity contour measurements along a streak<sup>(57,68)</sup> indicate that visual observation is not adequate to determine streak length. The FWHM of the streak along its long direction is much larger than the length observed visually. Nevertheless, a streak of considerable length is measured in many circumstances. We have already considered two possible contributions to the RHEED streak length, the finite instrument response and the cut of the Ewald sphere across the rod, but have discounted them as the principal causes of streak length for typical instruments and high-quality surfaces. Inelastic scattering will also contribute to streak length. RHEED measurements are usually made without any retarding bias; because no potential is applied to the fluorescent screen and, because it takes of the order of 1000 eV or more to excite the phosphor, the screen itself acts as a high-pass filter. Thus true secondaries do not contribute to the RHEED intensity. However, Kikuchi lines can cause significant intensity variations along or across a RHEED streak.<sup>(69)</sup> More importantly, it has been suggested that the length of RHEED streaks is due to the phonon scattering.<sup>(70)</sup> In this hypothesis, the extra momentum needed to get to a reciprocal-lattice rod when the  $\underline{S}$  vector no longer contacts the rods is provided by a phonon. This clearly should contribute to the length of the streak.

Measurements of the streak length at various temperatures indicate, however, that this effect is not significant.<sup>(68)</sup> The possibly most significant contributions to streak length come from defects such as steps or long-range curvature of the crystal surface.<sup>(68,71-73)</sup> Steps can cause considerable broadening of rods (see Fig. 9). A cut with the Ewald sphere at the appropriate conditions will lead to long streaks, while at slightly different angles of incidence a short streak or spot will be observed.<sup>(68)</sup> Long-range curvature may also be important.<sup>(71)</sup> Because the beam has a projected area on the sample that is quite large at grazing angles, areas with many slightly differing surface orientations (due to crystal mosaic) may participate in the diffraction. This will provide (Fig. 6b) a rod that gets increasingly broad with increasing  $G_{\perp}$ , allowing a long streak as the Ewald sphere passes through the rod. It was noted some years ago<sup>(71,72)</sup> that "good" surfaces gave short streaks or spots, a result that is being increasingly verified.<sup>(68)</sup> The various factors discussed above make it generally more difficult than in LEED to interpret a RHEED angular profile quantitatively and thus to exploit the greater resolving power that is available in RHEED.

#### D. Thermodynamics and Kinetics

As already indicated the easiest information obtainable through LEED or RHEED, simply by observing the diffraction pattern, is the size and shape of the surface or overlayer unit mesh. Because many overlayers (as well as some clean surfaces) form superlattices, investigation of the change in intensity and the appearance or disappearance of superlattice reflections in LEED or RHEED patterns as a function of coverage, temperature, or time gives an easy way to study

the thermodynamics of ordered phases and the kinetics of ordering or disordering. The most important measurement for these studies is simply the dependence of the diffracted-beam intensity on temperature. With the additional information on defects derived from the angular-profile measurements discussed in the last section, a complete study of overlayer phase transformations and ordering kinetics can be made, and the results of such studies can in principle be interpreted in terms of atom-atom interactions.<sup>(41)</sup>

Figure 20 shows a generic overlayer phase diagram that illustrates the main features to be expected for overlayers that can be treated within a lattice-gas model, i.e., a model in which the ordered state consists of overlayer atoms adsorbed commensurately into regular substrate lattice sites and the disordered state consists of the random placement of the adsorbed atoms into these sites. Incommensurate layers and commensurate-incommensurate transitions require more complex treatment. As can be seen, the generic phase diagram for a commensurate overlayer is the same as for a simple binary alloy that undergoes phase separation, the atoms in the overlayer forming one component and the vacancies the other. Thus coverage is analogous to composition. The major features are two-phase regions, consisting of coexisting ordered and "disordered" phases (the "disordered" phase being an ordered phase of vacancies), and one-phase regions, either ordered or "disordered". One-phase regions can have a width because a phase rich in one component can support a certain concentration of the other component before phase separation takes place. For overlayers, this means that at a given temperature the ordered overlayer can support a certain concentration of vacancies and the empty lattice (an ordered phase of vacancies) can

support a certain concentration of overlayer atoms. Transitions from a two-phase region to a one-phase region or vice versa are, by necessity, first-order, while transitions between one-phase regions may be first or second-order. It is necessary to distinguish between actual order-disorder transitions, such as point a, where one phase goes continuously or discontinuously into another, and disappearing - phase transformations, such as point c, where, as the temperature is increased, an ever smaller amount of a given phase exists, but where the order in that phase does not significantly change with temperature because the phase boundary is nearly vertical. Intermediate between these cases is point b, where both the amount of phase and the order in the phase change, with most of the change in order coming when only a little of the phase is left.

The most important measurement in phase transition experiments is the dependence of the Bragg intensity (the area under an angular profile) of a particular reflection on temperature, i.e.,  $J_{\text{beam}} J_{hk}(\theta, E) \text{ du vs } T$ , at various coverages. Three possible Bragg-intensity-vs-temperature plots for three different regions in the phase diagram are shown schematically in Fig. 20. It should be noted that the intensity can decay quite differently with temperature for different regions of the phase diagram. Angular-distribution measurements are useful in interpreting the temperature behavior and in identifying transition temperatures or equilibrium distributions of ordered phase. In order-disorder transitions, such as point a, no broadening of reflections should be observed until the transition temperature is reached. For disappearing - phase measurements, the reflections broaden continuously, but the broadening cannot be observed

until the physical width of the line exceeds the resolving power of the instrument. Usually this occurs at temperatures considerably lower than the temperature at which the phase first precipitates (or, conversely, disappears) for a given coverage. Instrument response affects the measured dependence of the Bragg intensity on temperature because the angular profile changes as the order changes. The measured intensity at any diffraction geometry is the convolution of the true intensity,  $I(\theta, E)$ , and the instrument response function,  $I(\theta, E)$ , (see Eq. 19). Accurate determination of intensity-decay profiles requires the deconvolution of the instrument response function from the measurement.<sup>(74)</sup> Measurements of "peak" intensities are meaningless unless it can be demonstrated that the angular profile is narrow compared to the instrument response function at all measurement temperatures. This can be true only for points on the phase diagram such as point a, where long-range order is preserved up to the transition temperature, where it vanishes.

Phase transition studies have general applicability to identification of the nature of the phase, including its geometric structure; the energetics that lead to the formation of a given phase, including adatom interactions and impurity stabilization; and the effect of defects or kinetic limitations on the formation or degree of order in a phase. Measurements of phase transitions between one-phase and two-phase regions are especially interesting from the point of view of adatom interactions, nucleation phenomena, and kinetics of ordering.

In the next section, the most important features of the instrumentation required to perform diffraction experiments are described, emphasizing the aspects of instrumental design that optimize a system for particular measurements.

#### V. Instrumentation and Sample Preparation

The major components of a diffractometer are a source, a sample goniometer, and a detector. In addition, for surface studies sample heating or cooling, a gas handling system or evaporation source, a mass spectrometer, and a separate gun for Auger electron spectroscopy are typically available. Schematic overall views of a LEED and a RHEED diffractometer are shown in Figs. 21 and 22. The focus of the discussion here will be on the gun, goniometer, and detector.<sup>(75)</sup> A brief discussion of sample preparation is also included.

##### A. Electron Guns

Electron guns used in diffractometers typically use electrostatic focussing and have a simple design, consisting of a thermionic cathode, an extraction electrode, an array of focussing electrodes, and electrostatic deflection plates for guiding the beam. Filaments are usually made of W or thoriated W, and may be hairpin wires or ribbons. Indirectly heated filaments (oxide, LaB<sub>6</sub>, etc.) are also used. In order to avoid background light and contamination of the sample due to evaporation from the filament, some electron guns have off-axis filaments. The thermionic cathode is situated in a Wehnelt cylinder, a can that completely surrounds the cathode except for the beam extraction aperture. The potential on the Wehnelt cylinder can be adjusted positive or negative with respect to the cathode, and is typically at nearly the same potential. Extraction of the beam is achieved with the

first electrode of a unipotential lens that then focusses the initially divergent beam. This lens forms an image of the true electron source, which may be part of the hairpin or the aperture of the Wehnelt cylinder, depending on the filament type, the filament current, and the potentials on the Wehnelt cylinder and the extraction electrode. Wehnelt cylinder and first-lens element apertures in low-energy guns are typically about 1 mm dia. or larger. The beam diameter can be decreased by reducing these aperture sizes. Small apertures give much reduced beam currents (e.g., inA at 100 eV for a 0.4 mm dia. first-lens aperture). For the 0.1  $\mu$ A beam currents required with commonly used detector schemes (grids and phosphor screen, or a simple Faraday cup), a minimum beam size of 200  $\mu$ m and a minimum divergence of 0.2° appear to be achievable at LEED energies with most common guns. Changing the bias on the Wehnelt cylinder with respect to the cathode drastically affects the beam current and its stability with energy, but does not affect the smallest achievable beam diameter at the focus conditions for typical current densities (less than 0.2 mA/cm<sup>2</sup>). At RHEED energies, spot sizes can be made much smaller.

Low-energy electron guns have not been optimized with respect to the parameters that give a high resolving power. Historically beam currents of 0.1  $\mu$ A in a spot of about 1/4 to 1 mm diameter with a beam divergence of 0.25° to 1° have been considered adequate for LEED. Wulfert and Henzler<sup>(76)</sup> have constructed a magnetically focussed gun to improve this situation. They use the concept of focussing with a long solenoid to produce small-diameter low-energy beams, with beam sizes of the order of 40  $\mu$ m<sup>(76)</sup> in the imaging plane. The magnetic field is along the beam direction. The magnetic field acts as a 1:1 lens that

images the crossover of the beam emerging from the Wehnelt cylinder of the gun onto the detector after reflection by the crystal. The corresponding minimum angle of resolution for normal incidence appears to be of the order of  $\theta_{\min} = 0.05^\circ$ , compared to values of the order of  $\theta_{\min} = 0.5^\circ$  obtainable in systems equipped with standard guns. Because of the small beam currents achievable with this gun, a detector with gain is used, which in this system<sup>(76)</sup> is a Faraday cup with a channeltron electron multiplier.

A recent development in low-energy electron guns is the use of field emission sources. The major advantages of a field emitter are its high luminosity and the fact that it is nearly a point source. The latter in principle makes a parallel beam a possibility. This can easily be visualized by considering a point source situated at the focus of a convergent lens. The high luminosity makes small beam sizes practical. Although field emitters have been used in high-energy-beam applications for some years, it has been difficult to make a low-energy beam without serious energy spread and angular divergence, because a high extraction potential is required with typical anode configurations. Because lenses are imperfect, the subsequent deceleration to low energies causes energy and angular spreading. A recent development<sup>(12)</sup> in anode configuration allows field emission at potentials as low as 150V, and perhaps lower. Currents as large as inA at 150 eV with beam sizes of less than 5 $\mu$ m have been achieved.<sup>(12)</sup>

Electron guns for RHEED applications operate at voltages anywhere from 5 kV to 100 kV. No particular effort has been made to optimize guns in this energy range for high resolving power, but even standard guns are likely to be better than low-energy guns because it is



generally easier to produce a finely focussed beam with small energy and angular spreads at higher energies. Various types of guns are in use; examples include guns from electron microscopes, guns in cylindrical mirror analyzers used for scanning Auger microscopy, and high-energy CRT guns.

#### B. Detectors

Signal detection in diffractometers requires the measurement of an energy and angle-resolved current. For LEED, a detector must be capable of 1) the measurement of a current of electrons at energies  $10 \text{ eV} < E_p < 1000 \text{ eV}$ , where  $E_p$  is the incident-beam energy; 2) energy resolution, i.e., the separation of those electrons at or very near  $E_p$  from the inelastically scattered electrons; and 3) angular resolution, i.e., the ability to separate the current in one diffracted beam from all the others, and to measure the angular distribution of current in one beam. For RHEED the energy range at which the detector operates is higher, but in principle, its capabilities must be the same as for LEED detectors. Two types of detectors are in common use, a Faraday cup that is mechanically driven and a fluorescent screen with or without a set of hemispherical grids. The most common LEED detector is the fluorescent screen with a set of nested grids. The inner grid is operated at the same potential as the sample, to provide a field-free region around the sample. The next grid (or two grids) is set at a negative bias to filter inelastically scattered electrons. The outermost grid is again operated at ground potential but is not needed for DC LEED operation. (If no intensities are to be measured, actually only two grids are required). The fluorescent screen is operated at several kV positive potential to give the electrons sufficient energy to excite the

phosphor. The major advantage of this detector is that it provides a visual display of essentially all the back-diffracted beams, making a rapid determination of the size and shape of the surface or overlayer unit mesh possible. On the other hand, the ability to give a visual display makes the fluorescent screen an inelegant detector from the point of view of signal processing. In many applications beam currents must be measured. Because the fluorescent screen changes an electron signal to an optical signal, reconversion to an electron signal is required.

Intensities in typical integrated-intensity-vs-energy profiles vary over three orders of magnitude, requiring a similar dynamic range for the fluorescent screen/detector combination. The response of a phosphor screen can be assumed to be linear over the ranges of beam currents used in LEED.<sup>(77)</sup> However, the dynamic range of the phosphor generally does not match that of detectors used to measure the optical intensity in a diffraction spot. Maxima in intensity-vs-energy profiles for typical incident-beam currents may saturate the detector. If the incident-beam current is reduced, the minima in intensity-vs-energy profiles become buried in fluorescent-screen noise, e.g., due to stray light or inelastic-scattering background. A fluorescent screen is therefore not ideal for measuring beam intensities quantitatively. In some applications absolute intensities are not required. For example, angular distributions are independent of beam current as long as the phosphor and the detector are not saturated. For such measurements, the fluorescent screen represents a detector with a very good response. Because the average phosphor particle size is typically of the order of micrometers, the phosphor acts like a detector with a continuously

movable, several  $\mu\text{m}$  wide aperture, which is so small that it contributes essentially nothing to the total instrument response. Of course, this optical signal must still be converted into electrons, and thus the aperture width of the light-sensitive detector must be included in the instrument response. The dynamic range must be high for this type of measurement.

An additional negative aspect of most standard fluorescent screens is that they are viewed in reflection, i.e., past the sample and through the grids. Aside from the fact the sample blocks part of the field of view and that the grids cause a loss of more than half the light intensity from the screen because of their limited transmission (each grid has typically 0.8 to 0.9 transmission), viewing in reflection generally requires the detector to be 20 to 30 cm from the screen. This causes a significant loss of intensity. Transparent fluorescent screens (glass coated with  $\text{SnO}_2$  and phosphor) have been used to avoid these problems. A light-sensitive detector can then be placed directly behind the screen.<sup>(57,78)</sup>

Spot telephotometers have commonly been used for recording the diffracted-beam intensity from fluorescent screens. It is difficult to follow the motion of diffraction spots on the screen with a photometer as the energy is varied, and used in the DC mode, a photometer lacks sensitivity. As a result, other methods of measuring the brightness of the fluorescent screen have been developed. To improve the sensitivity, Schrott et al.<sup>(79)</sup> have used a photodiode and synchronous detection, modulating the suppressor grid at 100 Hz. Background light is thus effectively removed. Stair et al.<sup>(80)</sup> recorded intensities by photographing the fluorescent screen at various diffraction conditions,

using high-speed 35 mm film. In this way the intensities of all reflections are obtained at the same time under identical conditions, a method far preferable, in terms of data reliability, to measuring the intensity-vs-energy profiles sequentially. The film is subsequently mechanically scanned and digitized using a computerized microdensitometer. A computer program locates the diffracted beams and provides an integrated intensity for each beam at each incident-beam energy. The time to develop and digitize the film is long, resulting in considerable delay between a measurement and the availability of the results of this measurement. A modification of the scanning procedure uses a vidicon camera interfaced to a minicomputer.<sup>(81,82)</sup> This reduces the delay time between measurement and availability of the results to about a day. An assessment of the sensitivity of this method has been made by Tommet et al.<sup>(82)</sup>

Photographing the screen leads to a reduction in total measurement time by introducing parallel detection, rather than the serial detection used in a telephotometer, but introduces no detector gain. A reduction in total exposure of one or two orders of magnitude (from  $10^{16}$  electrons/ $\text{mm}^2$  to  $10^{14}$  electrons/ $\text{mm}^2$  for a set of intensity-vs-energy curves for all observable beams) is achieved because of the parallel detection. However, measurements of the intensity of each reflection require the same incident-beam current and measurement time to achieve the same S/N ratio, <sup>where</sup> these measurements are obtained simultaneously or sequentially. Hence, in order to achieve a net gain in time, incident-beam currents must be of the same order of magnitude as for photometers. The use of photography can be eliminated by using a vidicon camera to view the fluorescent screen directly.<sup>(7,9)</sup> In this

detection system, the image on the screen is focussed onto the sensitive element of the vidicon tube, which consists of tracks that are divided into a large number of channels. The distribution of intensity in the channels of one track is accumulated into a memory array, with simultaneous subtraction of background light stored previously in a second array. This background-light measurement is made, for example, by biasing the electron gun so that the beam can't emerge or by turning off the screen voltage. The height of the track as well as the magnification of the optical system can be adjusted, effectively allowing changes in the detector dimensions relative to the intensity distribution on the screen. The contributions of the vidicon detector and lens to the instrument response have been measured and shown to be negligible compared to contributions from the electron beam.<sup>(9)</sup> Thus this type of detector scheme is excellent from the point of view of resolving power, although, as has been noted, the fact that grids are used affects the sensitivity and achievable S/N ratios because the background due to inelastically scattered electrons is large. In a direct application, a vidicon can only measure diffracted-beam profiles sequentially, but these can be made in real time. Despite the serial detection, the greater sensitivity of the vidicon relative to film gives about the same overall measurement time for a set of reflections. Delays in the availability of the data are eliminated because the data can be analyzed and displayed as they are taken.

The addition of a channel electron multiplier array<sup>(8)</sup> to the detector improves the sensitivity by introducing gain into the detector, but decreases the resolving power. The mean gain of a chevron (dual) channel electron multiplier array is of the order of  $10^6$ . Thus a

reduction in primary-beam current of  $10^6$  gives in principle the same S/N at the same measurement times. Because of the finite channel width, however, the channel plates produce a spatial broadening of the input signal. For chevron arrays this broadening is accentuated because the signal coming into one channel in the first plate gets spread into several channels in the second. For a negligibly small beam incident on a typical channel size of 25  $\mu\text{m}$ , the FWHM of the beam on the screen, after passing through the chevron plates, is about 75-100  $\mu\text{m}$ , at least double that of the vidicon/optics/fluorescent-screen combination. If the resolving power is of no concern (e.g., in intensity-vs-energy profiles, where an integral over the diffraction spot is in any case taken) this combination represents an excellent detector scheme. In angular-profile measurements the limited resolving power that results with this detector becomes important. Although the detector response can, of course, be deconvoluted from the measured intensity distribution, it is clear that the increased sensitivity of channel plates brings a reduction in ultimate spatial resolution.

Because channel plate arrays are usually flat, the distortion introduced in beams entering the plates at angles away from the normal to the plates must be taken into account.

The sensitivity of the detector can be further increased by replacing the fluorescent screen with a position-sensitive pulse detector. With a fluorescent screen biased at typical energies of 5 keV, the minimum measurable current (using a vidicon) is estimated to be 1000 pulses/sec. A position-sensitive detector can measure individual pulses. The first such detector that was constructed for LEED<sup>(10)</sup> consists of a resistive-anode encoder (RAE) preceded by a chevron

channel electron multiplier array. An RAE is a continuous resistive film that acts as a current divider for an incoming electron pulse, thus determining its spatial position. Although this type of detector determines the centroid of the arriving pulse, the spatial resolution is nevertheless not good. The spatial resolution is determined by the extent to which the thermal noise perturbs the pulse currents. Thus a trade-off between detector area and maximum allowable thermal noise occurs. For a 75 mm square RAE, the lateral resolution is estimated to be between 300 and 400  $\mu\text{m}$ <sup>(83,84)</sup>. The RAE can accommodate 50 kHz pulse rates. Data rates are therefore limited by the individual channel dead time in the channel plate array, and not by the RAE.

The ultimate presently attainable sensitivity and angular resolution are provided by a Faraday cup detector with a channel electron multiplier. With this arrangement individual pulses can be counted, and by making the aperture of the detector arbitrarily small, any degree of angular resolution can in principle be obtained. Such detectors are in common use in a variety of spectroscopic techniques, including LEED. Gronwald and Henzler<sup>(11)</sup> have described a Faraday cup detector that includes deflection plates in front of the aperture so that the beam profile can be measured without mechanical motion of the detector. Some Faraday cup detector designs contain no retarding grids but nevertheless provide much better energy resolution than is obtained with detectors incorporating retarding grids. Such detectors consist of a deep cup in close proximity to, but electrically isolated from, an aperture plate. The diameter of the cup is several times the diameter of the aperture, and the depth of the cup is several times its diameter. The cup is biased to within 1 to 2 eV of the energy of the

elastically scattered electrons. This detector provides excellent energy resolution (of the order of the thermal spread in the incident beam) without significant loss of secondary electrons from the cup. Because the fields outside the aperture are negligible, the angular distribution of electrons in the diffracted beam being measured is not disturbed. The advantage of good energy resolution is that inelastically scattered electrons can be eliminated to a much greater degree, making the background in angular profile measurements less of a problem. Finally, a Faraday cup detector is the only means of measuring analog signals quantitatively. Hence it is preferable for every diffractometer to have two detectors, the Faraday cup for quantitative current and high-angular-resolution measurements, and some form of position-sensitive parallel-output detector for the rapid data acquisition required for accurate structural determinations within the time or electron dose constraints of a typical surface crystallography experiment.

Detectors for RHEED have consisted in most cases simply of a fluorescent screen, although energy filtering and Faraday cups have been used.<sup>(71,72,85)</sup> RHEED measurements are always made in transmission through the screen, an advantage in terms of sensitivity. A light and position-sensitive probe has been used to measure RHEED beam profiles.<sup>(57)</sup> To eliminate variations in screen response, magnetic deflection of the diffracted beam has been used to scan the beam across a fixed detector.<sup>(68,72,85)</sup> RHEED measurements in scanning transmission electron microscopes are made with somewhat more sophisticated detection

schemes, such as a vidicon camera pickup from the fluorescent screen. In principle, all of the detection schemes discussed for LEED could as well be applied in RHEED.

#### C. Goniometers

The function of a goniometer is to position the crystal accurately with respect to the incident beam of electrons and the detector. The importance of such accuracy depends on the experiment being performed. For angular-profile measurements, absolute angles are not important. For intensity-vs-energy profiles, it is critical that absolute angles be well known and that the repeatability of setting these angles be excellent. Although they are not very precise, standard UHV manipulators are commonly used for all types of diffraction measurements.

Goniometers for special purposes have been built. An exceedingly precise one<sup>(86)</sup> was constructed to perform automatically constant-momentum-transfer-averaging<sup>(61,62)</sup> of intensities. The goniometer is constructed to couple the motions of the Faraday cup and the crystal in colatitude, so that the momentum transfer vector automatically remains constant as the diffraction conditions are varied. Uncoupling of the motions is also possible to permit arbitrary angles of incidence and diffraction.

For fine-beam or scanning LEED applications it is also necessary that the goniometer be stable against vibrations. For such applications, modified versions of manipulators used for scanning Auger spectroscopy or similar techniques can be used.

#### D. Sample Preparation

Sample preparation is extremely important in surface crystallography experiments. The magnitude of the problem can be appreciated when it is realized that the outer few atomic layers provide all the structural information. It may seem surprising that any surface can be prepared well enough to observe diffraction, until one remembers that the resolving power of typical instruments is only on the order of several hundred Å. Thus surfaces that have ordered regions that are this large on the average appear "perfect" to the diffractometer. More importantly, ordered regions that are on the average much smaller than 100 Å still give good diffraction pictures. Ordered regions as small as a few atoms across give a measurable diffraction pattern if there are enough of them. Thus the surface order does not need to be very good if there is underlying crystallinity to provide orientational and translational coherence between the ordered regions. Much of the surface can be covered with scratches, etch pits, and so forth, and these will not (superficially at least) affect the diffraction pattern, especially when the instrument has a low resolving power.

Nevertheless it is quite difficult to prepare surfaces for diffraction experiments. The best surfaces, as regards low defect density and cleanliness, are cleavage faces of crystals that can be cleaved in vacuum. These include a number of semiconductor crystals and the layer compounds. Such surfaces can be used to measure the instrument response. Most crystals do not cleave readily. Thus the materials and surface orientations that can be studied by cleaving in vacuum are quite limited. Most surfaces require extensive preparation. This includes orienting, polishing, and etching before

further treatment in vacuum. Orientation to the desired axis to within  $0.5^\circ$ , using Laue back-reflection, is common practice; with the use of a stable multiaxis goniometer<sup>(87)</sup> and repeated attempts at polishing, accuracy to  $< 0.1^\circ$  can be achieved. Frequently polishing results in surface curvature near the edges of the crystal, resulting in an apparent misorientation effect there. Thus care must be taken to use only the center of the crystal surface or to prepare a large-area surface for diffraction studies. The surface produced by polishing is so damaged that no diffraction pattern is observable, generally even with x-rays. Subsequent etching removes the polishing damage to a sufficient degree to observe diffraction and also exposes the crystal mosaic, which may range in metals from a fraction of a degree to several degrees for poorly grown crystals. A wide variety of etch and polishing procedures exists for different materials.<sup>(88)</sup>

At the stage of introduction into the vacuum chamber there is still remanent surface damage and also a contaminant layer that frequently consists of an oxide or a carbonaceous deposit. These can be removed by thermal, chemical, or physical treatments, or a combination of any of them.<sup>(89)</sup> Thermal annealing is usually insufficient by itself to clean the surface, because of the tenacity of the contaminant layers. A combination of chemical and heat treatment is the gentlest and most satisfactory method, from the point of view of surface defects, of preparing the surface. It is also exceedingly slow. Generally an oxidation for large periods of time is required to remove carbon from the surface and to deplete the near-surface regions of carbon, as it continues to diffuse to the sink that is provided by the surface. Oxidation leaves the surface with an oxide or at least a layer of

chemisorbed oxygen. Oxygen may also have diffused into the lattice. A reduction in hydrogen can remove the oxygen. The hydrogen itself may be desorbed simply by heating. The resulting surface generally has good crystallinity, although it may still contain a large number of macroscopic defects, such as etch pits, scratches, etc. Thus the area that participates in the diffraction is less than the total surface area, as can be observed in noble-gas dosing experiments.<sup>(90)</sup> Repeated heat treatments, required, for example, to renew a surface after a chemisorption experiment, frequently accentuate gross defect structure, so that the surface may look exceedingly rough and nonspecular after a period of continued use.

The second major in-situ surface preparation technique is physical removal of the surface contamination or damaged layers by sputter etching with subsequent annealing. Surfaces prepared in this manner always have remanent damage, with a defect structure that is rather fine-scale and frequently observable in the diffraction pattern as a broadening of the angular profiles or an increase in background. Generally such damage cannot be annealed out in reasonable laboratory times. Noble gases that are used for sputtering are trapped in the lattice to depths of many tens of  $\text{\AA}$  or more<sup>(91)</sup>, causing displacement of atoms from regular lattice sites, strain, and dislocations. Surfaces are frequently left with a step structure and a nonequilibrium concentration of point defects that are difficult to eliminate. These defects can markedly affect a number of diffraction measurements, especially measurements of the thermodynamics and kinetics of overlayer

ordering. Thus sputter etching should not be used on surfaces intended as substrates for such experiments, unless the purpose is to study the influence of defects on ordering.

Surfaces can, of course, also be grown in-situ, by molecular-beam epitaxy. These can be macroscopically much smoother than polished surfaces. Insufficient work has been done with diffraction on such surfaces to ascertain whether, in fact, the density of atomic-scale defects can also be made lower than on polished or cleaved surfaces. The fact that many of these films are grown at conditions far from equilibrium suggests that they may have a relatively large concentration of structural defects.

#### VI. Representative Experimental Results

In this section we very briefly illustrate the discussion of the different types of measurements with examples that are representative of the data that can be expected with typical LEED and RHEED instrumentation. Rather than presenting "finished" results, we emphasize data as they appear directly in the measurement.

Measurements of the integrated intensity vs. energy in LEED have been made mainly with either a fluorescent screen/grid detector or a Faraday cup. Figure 23 shows a comparison of "intensity-energy" profiles of  $W(100)$  taken in both ways.<sup>(9)</sup> The agreement between the curves is typical for data taken at different times, with different detectors, or in different laboratories. The differences in peak positions or peak intensities are probably due to the sensitivity of integrated-intensity vs energy profiles to the angle of incidence, with even a fraction of a degree causing significant changes in a profile. The rising intensity in the peaks and background of the curve taken from

the fluorescent screen is probably caused by the larger inelastic-scattering background accepted by this detector relative to that accepted by the Faraday cup. Such curves are taken at a series of different incident angles and for several diffracted beams and then compared to dynamical calculations<sup>(16,17)</sup>. The order of magnitude of experimental uncertainties involved in equilibrium position determination is illustrated in Fig. 23. Added to this are the uncertainties in parameters entering into the calculations and the difficulty, mentioned earlier, of defining satisfactory reliability factors. The present status of equilibrium position determinations appears to be that, while the precision of calculations may be as good as 0.01 Å in the best cases, the absolute accuracy of structure determinations is probably no better than 0.03 Å.

Angular-profile measurements in LEED are illustrated in Figure 24, which shows an angular scan over four orders of reflection from cleaved GaAs (110) and GaAs (110) that has been sputter-etched and only partially reordered by annealing and thus contains many steps.<sup>(92)</sup> The broadening of the reflections from the sputter-etched surface is evident. The spectra were taken at a diffraction condition at which the amplitudes scattered from the different terraces were out of phase (i.e., near a value of  $G_{\perp}$  at which the rods in Fig. 9 are broadest). The curves represent an average of 30 scans requiring 1 min.<sup>(92)</sup> Figure 25 shows expanded scans of two profiles taken over identical measurement times from the sputter-etched GaAs (110) surface annealed at two different temperatures.<sup>(92)</sup> The change in the profile width and shape is evident. The signal-to-noise ratio can differ markedly for the two curves, as expected. A complete two-dimensional angular profile of a

diffraction spot (11) is shown in Fig. 26. It was determined by repeated scans, each slightly displaced from the previous one, of a very-small-aperture detector across the diffracted beam. Low-intensity wings are observed around the main peak. The full width at half-maximum of such angular profiles taken at a variety of  $G_{\perp}$  values (i.e., at different energies) and for several beams is generally used to determine step heights and extract surface step densities<sup>(25,26,43)</sup>, average overlayer island sizes,<sup>(21,40,93,94)</sup> or other surface defects.<sup>(49)</sup> The complete angular profile can be used to determine the size distribution of ordered islands or terraces, rather than just the average size.<sup>(26,53)</sup> The uncertainty in angular profile measurements is typically not better than 5% of the signal, with the resolving power depending on the instrument response. In the best cases, the resolving power may be 5,000 to 10,000 Å. The fitting of complete angular profiles with model calculations is still in its initial stages, and thus there can be, at present, only little confidence even in the uniqueness of overlayer and surface defect structure determinations. As better models are developed, a rapid improvement in the quantitative nature of structural defect determinations can be expected.

RHEED measurements of angular profiles are illustrated in Fig. 27, which shows contour maps of RHEED streaks for the ordering of a GaAs layer deposited onto a GaAs (001) surface.<sup>(57)</sup> The contour maps show that for longer ordering times the streaks are becoming shorter and turning into spots, indicating increased order in the overlayer. Similar measurements are being made on stepped surfaces.<sup>(68)</sup> Models being developed for defect structure analysis are, of course, equally applicable to RHEED data.

Intensity-temperature measurements used to determine both mean square vibrational amplitudes in surfaces and the positions of phase boundaries are illustrated in Fig. 28. The temperature decay of the "peak" intensity of the (1/2,1/2) superlattice reflection for saturation coverage of a  $M(110)p(2 \times 1)-O$  layer<sup>(74)</sup> is plotted along with the change in width of the angular profile. Both the measured intensity and the intensity corrected for instrument response are shown. The Debye-Waller factor has not been accounted for. It is given by a straight-line fit to the data at low temperatures. The deviation from this straight line indicates a phase transition. Such measurements are repeated at various coverages (see Fig. 20) to establish the boundaries in the overlayer phase diagram. Measurements at various energies and for various beams give the  $|S|$  dependence of the Debye-Waller factor, but should all give the same position of the phase boundary at a given coverage. A careful analysis of the shape of the intensity decay curve can furthermore provide information on finite-size effects, correlation lengths, and the nature of the phase transition, including the determination of the order of the transition<sup>(86)</sup> and the values of critical exponents.<sup>(95)</sup> Intensity-temperature and angular profiles can also be observed dynamically as a function of time at fixed coverage and temperature to follow the growth of an overlayer or surface phase. From the behavior of the width and maximum intensity with time at different temperatures it is then in principle possible to determine activation energies and preexponential factors, as well as the growth law operative for the ordered structure.

Intensity-temperature measurements have been made for a number of years, initially to determine the Debye-Waller factor and thermal-



diffuse-intensity for clean surfaces and later to determine phase diagrams for overlayers. Debye-Waller factor measurements are difficult to interpret in terms of surface vibrational amplitudes because of the finite and exponentially decaying penetration of the electron beam. Few phase diagram measurements have been made. Difficulties lie in the interpretation of the temperature decay in terms of the position of the phase boundary at different coverages, as illustrated in Fig. 20, and the relationship between the diffracted intensity and the existing order on the surface.

#### VII. Conclusions

In this chapter, we have attempted, in a tutorial fashion, to provide the basic elements necessary for an understanding of surface-sensitive diffraction techniques. The emphasis has been on those aspects that will help the reader evaluate the power, as well as the limitations, of diffraction techniques to study surface crystallography. Much of what has been said in the early sections of this chapter is also applicable to grazing-incidence x-ray diffraction and to atomic-beam diffraction, although they have not been explicitly mentioned. Of necessity, a number of other techniques have not been discussed. One of these, the measurement of surface extended-x-ray-absorption fine structure (EXAFS), a potentially quite powerful diffraction technique, can be used to determine the local structural environment (i.e., nearest-neighbor distances) around individual types of surface atoms. It is based on measuring the diffraction of a spherical wave that represents a photoelectron (or a core level electron excited by any other technique) emitted from a particular type of atom. The resulting intensity as a function of momentum transfer can be

evaluated as in the early parts of this chapter. The major difficulties with the technique appear to be the extremely small signal levels and the limited range in momentum transfer that is accessible, leading to relatively large uncertainties in the determination of the positions of the nearest-neighbor atoms.

Limited surface crystallography information is also provided by other techniques that are not related to diffraction. They are too numerous to mention here. The most important of them are ion-beam techniques, which are reviewed elsewhere in this book.

Finally, a review of the experimental aspects of a technique or class of techniques should provide an evaluation of the state of the art as well as a prognosis for the future. In our view, the development of technology for surface-sensitive diffraction has lagged considerably behind that of other surface analysis techniques. This is now beginning to change, as the importance of high-quality, quantitative structural information in the interpretation and evaluation of the output of surface spectroscopies is becoming increasingly apparent. One can expect the significant advances in detection schemes, efficiency, and resolving power in LEED and RHEED, as well as an overall improvement in the quality of RHEED systems and in their response. One can also expect application of these techniques to a widening range of problems, as well as a recognition of the necessity of understanding instrumental parameters to obtain truly quantitative information. A further impetus to this development is the recent marriage of surface science and ultrahigh-vacuum technology with high-energy electron microscopy and diffraction, a field at the forefront of technology in which the ideas of instrumental response, data quality, and quantitative interpretation

of results are firmly established. It is likely that this union will bring significant advances both in our understanding of surface crystallography and in the development of experimental techniques.

#### VIII. Acknowledgements

I would like to acknowledge discussions that have aided my understanding of various aspects of diffraction with D. Savage, D. Saloner, J. Martin, T.-M. Lu, P. I. Cohen, M. Henzler, and M. B. Webb. Work described in this chapter that was performed here was supported in part by NSF under Grant No. DMR 78-25754 and in part by ONR. I thank the several graduate students who have been responsible for the performance of the actual work. Finally it is a pleasure to thank Ms. Lynn Kendall for typing this manuscript and its several progenitors, H. M. Clearfield, D. Savage, and D. Saloner for proofreading it, and J. Bohlman for making the drawings.

#### REFERENCES

1. C. J. Davisson and L. H. Germer, *Phys. Rev.* **30**, 705 (1927).
2. W. F. Sproull, *Rev. Sci. Instrum.* **4**, 193 (1933).
3. W. Ehrenberg, *Phil. Mag.* **18**, 878 (1934).
4. J. J. Lander, J. Morrison, and F. Unterwald, *Rev. Sci. Instrum.* **33**, 782 (1962).
5. C. W. Caldwell, *Rev. Sci. Instrum.* **36**, 1500 (1965).
6. R. L. Park and M. E. Farnsworth, *Rev. Sci. Instrum.* **35**, 1592 (1964).
7. P. Heilmann, E. Lang, K. Heinz, and K. Müller, *Appl. Phys.* **9**, 247 (1976); E. Lang, P. Heilmann, G. Hanke, and K. Müller, *Appl. Phys.* **19**, 287 (1979).
8. M. D. Chinn and S. C. Fain, *J. Vac. Sci. Technol.* **14**, 314 (1977).
9. D. G. Welkie and M. G. Legally, *Appl. Surface Sci.* **3**, 272 (1979).
10. P. C. Stair, *Rev. Sci. Instrum.* **51**, 132 (1980).
11. K. D. Gronwald and M. Henzler, *Surface Sci.* **117**, 180 (1982).
12. J. A. Martin and M. G. Legally, *J. Vac. Sci. Technol.* **A1**, 1210 (1983).
13. E. G. McRae, *J. Chem. Phys.* **45**, 3258 (1966).
14. C. B. Duke and C. W. Tucker, Jr., *Surface Sci.* **15**, 231 (1969).
15. D. W. Jepsen, P. M. Marcus, and F. Jona, *Phys. Rev.* **B5**, 3933 (1972); **B6** 3684 (1972).
16. J. B. Pendry, *Low-Energy Electron Diffraction* (Academic Press, New York, 1974).
17. M. A. Van Hove and S. Y. Tong, *Surface Crystallography by LEED* (Springer, Berlin, 1979).
18. R. L. Park, *J. Appl. Phys.* **37**, 295 (1966).
19. P. J. Estrup and J. Anderson, *Surface Sci.* **B**, 101 (1967).

20. W. P. Ellis and R. L. Schwoebel, *Surface Sci.* 11, 82 (1968).
21. J. C. Tracy and J. M. Blakely, *Surface Sci.* 15, 257 (1969); J. C. Tracy, Ph.D. dissertation, Cornell University (1968, unpublished).
22. J. E. Houston and R. L. Park, *Surface Sci.* 21, 209 (1970); 26, 269 (1971).
23. C. S. McKee, D. L. Perry, and M. W. Roberts, *Surface Sci.* 39, 176 (1973).
24. M. Henzler, *Surface Sci.* 22, 12 (1970).
25. M. Henzler, in *Electron Spectroscopy for Surface Analysis*, ed. H. Ibach, *Topics in Current Physics*, Vol. 4 (Springer, Berlin, 1977).
26. T.-M. Lu and M. G. Lagally, *Surface Sci.* 120, 42 (1982).
27. T.-M. Lu, L.-H. Zhao, M. G. Lagally, G.-C. Wang, and J. E. Houston, *Surface Sci.* 122, 519 (1982).
28. J. J. Lander, *Progress in Solid State Chemistry* 2, 26 (1965).
29. J. J. Lander and J. Morrison, *J. Appl. Phys.* 34, 3517 (1963).
30. P. J. Estrup, in *Modern Diffraction and Imaging Techniques in Materials Science*, eds. S. Amelinckx, R. Gevers, G. Remaut, and J. Van Landuyt (North Holland, Amsterdam, 1970).
31. J. W. May, *Adv. Catalysis* 21, 152 (1970).
32. P. J. Estrup and E. G. McRae, *Surface Sci.* 25, 1 (1971).
33. G. A. Somorjai and H. H. Farrell, *Adv. Chem. Phys.* 20, 215 (1972); G. A. Somorjai, *Surface Sci.* 34, 156 (1973).
34. M. B. Webb and M. G. Lagally, *Solid State Phys.* 28, 301 (1973).
35. G. Ertl and J. Küppers, *Low-Energy Electrons and Surface Chemistry*, (Verlag Chemie, Weinheim, 1974), chs. 9 and 10.
36. J. A. Stozier, Jr., D. W. Jepsen, and F. Jona, in *Surface Physics of Materials*, ed. J. M. Blakely, (Academic, New York, 1975).

37. M. G. Lagally, *ibid*
38. F. Jona, *J. Phys. C*, 11, 4271 (1978).
39. M. A. Van Hove, in *The Nature of the Surface (Chemical) Bond*, eds. T. N. Rhodin and G. Ertl, (North-Holland, Amsterdam, 1979).
40. M. G. Lagally, G.-C. Wang, and T.-M. Lu, in *Chemistry and Physics of Solid Surfaces*, Vol. II (CRC, Boca Raton, FL, 1979).
41. M. G. Lagally, T.-M. Lu, and D. G. Melkie, *J. Vac. Sci. Technol.* 17, 233 (1980).
42. G. A. Somorjai, J. E. Crowell, R. J. Koestner, L. H. Dubois, and M. A. Van Hove, in *Proceedings of the 9th Int. Conf. on Atomic Spectroscopy*, Tokyo, (1981).
43. M. Henzler, *Appl. Surface Sci.* 11/12, 450 (1982).
44. M. G. Lagally, *Appl. Surface Sci.* 13, 260 (1982).
45. M. G. Lagally, in *Chemistry and Physics of Solid Surfaces*, Vol. IV, eds. R. Vanselow and R. Howe, *Springer Series in Chemical Physics*, Vol. 20, (Springer, Heidelberg, 1982).
46. M. G. Lagally and J. A. Martin, *Rev. Sci. Instrum.* xx, xxx (1983).
47. J. J. Lander and J. Morrison, *J. Appl. Phys.* 34, 3517 (1963), E. R. Jones, J. T. McKinney, and M. B. Webb, *Phys. Rev.* 151, 476 (1966); Ref. 34.
48. D. G. Melkie, Ph.D. dissertation, University of Wisconsin-Madison (1981, unpublished); D. G. Melkie and M. G. Lagally, *Thin Solid Films* 93, 219 (1982).
49. D. G. Melkie, M. G. Lagally, and R. L. Palmer, *J. Vac. Sci. Technol.* 17, 453 (1980).
50. H. M. Clearfield, D. G. Melkie, T.-M. Lu, and M. G. Lagally, *J. Vac. Sci. Technol.* 19, 323 (1981).

51. S. C. Fain and M. D. Chinn, *J. de Physique* **38** Suppl 10, C4-99 (1977).
52. S. Semancik and P. J. Estrup, *J. Vac. Sci. Technol.* **18**, 541 (1981); R. A. Barker and P. J. Estrup, *J. Chem. Phys.* **74**, 1442 (1981); Ref. 32.
53. D. A. Saloner and M. G. Lagally, *Bull. Am. Phys. Soc.* **28**, 457 (1983); in preparation.
54. See, for example, K. R. Spangenberg, *Fundamentals of Electron Devices*, (McGraw-Hill, New York, 1957); R. L. Park, in *Experimental Methods in Catalytic Research*, vol. III, eds. M. Dawson and C. A. Anderson, (Academic, New York, 1976).
55. T. M. Lu and M. G. Lagally, *Surface Sci.* **99**, 695 (1980).
56. R. L. Park, J. E. Houston, and D. G. Schreiner, *Rev. Sci. Instrum.* **42**, 60 (1971).
57. J. M. Van Hove, P. Pukite, P. I. Cohen, and C. S. Lent, *J. Vac. Sci. Technol.* **A1**, 609 (1983).
58. D. E. Savage and M. G. Lagally, in preparation.
59. T.-M. Lu, M. G. Lagally, and G.-C. Wang, *Surface Sci.* **104**, L 229 (1981).
60. For a summary, see M. A. Van Hove, in *Surface Structure by LEED*, ed. P. M. Marcus, (Plenum, 1984, to appear).
61. M. G. Lagally, T. C. Ngoc, and M. B. Webb, *Phys. Rev. Letters* **26**, 1557 (1971).
62. T. C. Ngoc, M. G. Lagally, and M. B. Webb, *Surface Sci.* **35**, 117 (1973).
63. J. T. McKinney, Ph.D. dissertation, University of Wisconsin-Madison (1966, unpublished), J. T. McKinney, E. R. Jones, Jr., and M. B. Webb, *Phys. Rev.* **160**, 523 (1967).
64. R. F. Barnes, M. G. Lagally, and M. B. Webb, *Phys. Rev.* **171**, 627

65. M. G. Lagally and M. B. Webb, in *The Structure and Chemistry of Solid Surfaces*, ed. G. A. Somorjai, (Wiley, New York, 1969) ch. 20.
66. Phonon dispersion relations have been measured with high-resolution electron energy loss spectroscopy: S. Lehwald, J. M. Szeftel, H. Ibach, T. S. Rahman, and D. L. Mills, *Phys. Rev. Letters* **50**, 518 (1983).
67. R. L. Dennis and M. B. Webb, *J. Vac. Sci. Technol.* **10**, 192 (1973).
68. J. M. Van Hove, C. S. Lent, P. R. Pukite, and P. I. Cohen, *J. Vac. Sci. Technol.* **B1**, 741 (1983).
69. P. I. Cohen, private communication.
70. S. Holloway and J. L. Beeby, *J. Phys. C* **11**, L247 (1978); J. L. Beeby, *Surface Sci.* **80**, 56 (1979); S. Holloway, *Surface Sci.* **80**, 62 (1979).
71. J. F. Menadue, *Acta Cryst.* **A28**, 1 (1972).
72. D. B. Dove, R. Ludeke, and L. L. Cheng, *J. Appl. Phys.* **44**, 1897 (1973).
73. J. M. Cowley, *Ultramicroscopy* **9**, 291 (1982); private communication.
74. G.-C. Wang, T.-M. Lu, and M. G. Lagally, *J. Chem. Phys.* **69**, 479 (1978).
75. For a detailed discussion of LEED instrumentation, see Reference 46.
76. F.-M. Wulfert, Ph.D. dissertation, University of Hannover, (1982, unpublished). Ref. 43.
77. A. Brill and F. A. Kröger, *Phillips Tech. Rev.* **12**, 120 (1950).
78. P. A. Bennett and M. B. Webb, private communication; L. de Bersuder, *Rev. Sci. Instrum.* **45**, 1569 (1972).
79. A. G. Schrott, M. D. Chinn, C. G. Shaw, and S. C. Fain, Jr., *J. Vac. Sci. Technol.* **21**, 101 (1982).

80. P. C. Stair, T. J. Kaminska, L. L. Kesmodel, and G. A. Somorjai, *Phys. Rev.* **B15**, 623 (1975).
81. D. C. Frost, K. A. R. Mitchell, F. R. Shepherd, and P. R. Watson, *J. Vac. Sci. Technol.* **13**, 1196 (1976).
82. T. N. Tommet, G. B. Olszewski, P. A. Chadwick, and S. L. Bernasek, *Rev. Sci. Instrum.* **50**, 147 (1979).
83. M. Lampton and F. Paresce, *Rev. Sci. Instrum.* **45**, 1098 (1974).
84. H. O. Anger, *Instrum. Soc. Am. Trans.* **5**, 311 (1966).
85. M. F. Tompsett and C. W. B. Grigson, *J. Instrum. Sci.* **43**, 430 (1966); M. F. Tompsett, *J. Mat. Sci.* **7**, 1069 (1972).
86. P. A. Bennett, Ph.D. dissertation, University of Wisconsin-Madison (1980, unpublished); P. A. Bennett and M. B. Webb, *Surface Sci.* **104**, 74 (1981).
87. W. L. Bond, *J. Sci. Instrum.* **38**, 63 (1961); J. F. Wendelken, S. P. Withrow, and C. A. Foster, *Rev. Sci. Instrum.* **48**, 1215 (1977).
88. See, for example G. Petzow, *Metallographic Etching*, ASM, Metals Park, OH (1978); F. Rosebury, *Handbook of Electron Tube and Vacuum Techniques*, Addison-Wesley, Reading, MA (1965).
89. A summary of vacuum cleaning treatments for wide range of materials is given by R. G. Musket, M. McLean, C. A. Colmenares, D. M. Makowiecki, and W. J. Siekhaus, *Appl. Surface Sci.* **10**, 143 (1982).
90. M. B. Webb, private communication.
91. Trapping of Ar from the sputter etching process has been observed with Rutherford ion backscattering measurements. I. Feldman, private communication.
92. H. M. Clearfield, unpublished. H. M. Clearfield, D. Saloner, and M. G. Legally, *J. Vac. Sci. Technol.*, submitted.

93. P. O. Hahn, J. Clabes, and M. Henzler, *J. Appl. Phys.* **51**, 2079 (1980).
94. G. C. Wang, Ph.D. dissertation, University of Wisconsin-Madison (1978, unpublished). M. G. Legally, T.-M. Lu, and G.-C. Wang, in *Ordering in Two Dimensions*, ed. S. Sinha (Elsevier-North Holland, Amsterdam, 1980).
95. R. L. Park, T. L. Einstein, A. R. Kortan, and L. D. Roelofs, in *Ordering in Two Dimensions*, ed. S. Sinha, (Elsevier-North Holland, Amsterdam, 1980).

## Figure Captions

Fig. 1 Reciprocal lattice and Ewald construction for a crystal illuminated by penetrating radiation. a) Diffraction geometry and energy appropriate for LEED; b) diffraction geometry and energy appropriate for RHEED. The relationship between the separation of reciprocal-lattice points and the length of the  $\underline{k}$  vectors corresponds to a lattice with 3 Å lattice constant and energies of 150 eV and 10,000 eV respectively.

Fig. 2 Reciprocal lattice for a single plane of atoms and Ewald construction for a) LEED and b) RHEED geometries. The relationship between the separation of rods and the lengths of the  $\underline{k}$  vectors corresponds to a lattice with 3 Å row spacing and energies of 150 eV and 10,000 eV respectively. The intersection of the Ewald sphere and reciprocal-lattice rod in b) is misleading. The widths of the lines for both the Ewald sphere and the reciprocal-lattice rod vastly exceed physically realistic values.

Fig. 3 Reciprocal lattice and Ewald construction for a crystal illuminated by weakly penetration radiation. The reciprocal lattice is generally drawn as a set of rods with the positions of the third Laue condition indicated. The Ewald construction is drawn appropriate for LEED. The variation of the interference function with  $G_{\perp}$  along a rod is indicated on the right. The real lattice to which this reciprocal lattice corresponds is shown on the bottom.

Fig. 4 Dependence of the mean free path of electrons for inelastic scattering,  $\lambda_{inel}$ , on their kinetic energy. The hatched area indicates the range of values of  $\lambda_{inel}$  that have been measured for different materials.

Fig. 5 Cut in the  $\underline{a}$  direction through the reciprocal lattice of a two-dimensional crystal that contains random lattice strain in the  $\underline{a}$  direction. The reciprocal-lattice rods broaden with increasing order,  $n$ , of reflection. The hatched regions represent the full width at half maximum of the intensity distribution. The (00) rod is not sensitive to strain broadening. The widths are greatly exaggerated.

Fig. 6 Schematic illustration of mosaic structure in a crystal and the reciprocal lattice corresponding to the surface. a) Mosaic structure, with an average misorientation angle,  $\alpha$ . The misorientation is vastly exaggerated. b) Cut in the  $\underline{a}$  direction through the corresponding reciprocal lattice, which consists of many reciprocal lattices all with a common origin but misoriented with respect to each other by the angle  $\alpha$ . The crystallite size is assumed large enough to produce narrow rods as shown.

Fig. 7 Cut in the  $\underline{a}$  direction through the reciprocal lattice of a vicinal surface with monotonically increasing steps and a constant terrace size. a) Surface:  $a$  is the row spacing,  $d$  the plane spacing, and  $L$  the separation of terraces, b) reciprocal lattice: the narrow rods represent the reciprocal lattice of a lattice whose unit vector is  $L$ . The separation of rods and their inclination depend on the terrace size  $L$ . The hatched

rods represent the reciprocal lattice of a finite lattice (each terrace) whose unit vector is  $a$ . The complete reciprocal lattice for each terrace, called the terrace structure factor, is shown above the figure. Diffraction features occur when the product of the two reciprocal lattices is nonzero. The period in the appearance of diffraction features gives the inverse of the layer spacing,  $d$ . The figure is drawn for a terrace size of 5 atoms.

Fig. 8 Cut in the  $a$  direction through the reciprocal lattice of a stepped surface with constant terrace size and steps alternately up and down. a) Surface, b) two structure factor components, c) complete reciprocal lattice.  $|F_1|^2$  is the structure factor of the (infinite) lattice whose unit mesh vector is  $10a$ .  $|F_2|^2$  is the structure factor of a single terrace (five rows wide) with unit mesh vector  $a$ . The complete reciprocal lattice consists of delta-function rods that have zero intensity at periodic positions in  $G_{\perp}$ . The blackness of the lines is meant to illustrate the intensity. The periodicity reflects the inverse of the layer spacing. The periods in panel c) are not in scale with the lattice periodicity shown in panel a).

Fig. 9 Cut in the  $a$  direction through the reciprocal lattice for a surface with AB stacking that has random up and down step edges occurring at random intervals. a) Surface, b) reciprocal lattice. The hatched regions represent the FWHM of the

intensity distribution. This width is related to the average terrace size. The periodicity in  $G_{\perp}$  reflects the inverse of the step height.

Fig. 10 Cut in the  $a$  direction through the reciprocal lattice for a surface with AB stacking that contains a wide distribution of step heights that are multiples of the monatomic-step height.

Fig. 11 Cuts in the  $a$  direction through reciprocal lattices for a  $p(2 \times 1)$  overlayer on an infinite, perfectly ordered substrate. The overlayer atoms are assumed to sit in bridge sites, so that the layer and substrate appear to form an AB stacking sequence. a) Complete, infinite, and perfectly ordered overlayer. Sharp half-order rods appear. b) Low-coverage overlayer broken up into finite-size islands. Upper panel: cut at a particular  $G_{\perp}$ . Lower panel: behavior as a function of  $G_{\perp}$ . The hatched areas represent the FWHM. The half-order rods are broad and the fundamental reflections contain a diffuse-intensity halo. Its behaviour with  $G_{\perp}$  depends on the scattering phase shift differences between overlayer and substrate atoms and on the overlayer-substrate distance. The width and shape of the superlattice rods are related to the average island size and the size distribution. c) Saturation-coverage overlayer with antiphase domain boundaries. Upper and lower panels as in b). The superlattice reflections are broad as in b). Their width and shape reflect the average domain size. The fundamental reflections do not have a diffuse-intensity halo.

Fig. 12 Schematic diagram of an overlayer containing a twin boundary and the resulting reciprocal lattice. a) Surface: Overlayer atoms on one side of the twin boundary occupy sites that are displaced by  $1/3$  of a substrate lattice constant. b) Cut in the  $a$  direction through the corresponding reciprocal lattice. The hatched areas represent the FWHM. Every third rod is not sensitive to the twin boundary, because all atoms scatter in phase. Other rods broaden and reflect the twin size distribution. Relatively thick overlayers are assumed so that there is no interference with the substrate. The upper panel shows a cut at a particular  $G_{\perp}$ . From Ref. 48.

Fig. 13 Cut in the  $a$  direction through the reciprocal lattice corresponding to a layer that consists of ordered regions that are translationally random in the  $a$  direction. The layer is assumed thick enough so that no interference with the substrate occurs. The upper panel shows a cut at a particular  $G_{\perp}$ .

Fig. 14 Schematic diagrams in real and reciprocal space illustrating various contributions to instrumental broadening. a) Energy spread (either in the incident beam or due to detector resolution), (00) reflection. Integration over a range in  $G_{\perp}$  occurs, but no spread in  $G_{\parallel}$ . b) Energy spread, nonspecular reflections. An integration over a range in  $G_{\perp}$  and a spreading in  $G_{\parallel}$  result. c) Angular divergence, for a beam focussed on the detector. An integration over a range in  $G_{\perp}$  results, but, because the particular beam (here chosen to be (00)) was focussed on the detector, there is no uncertainty in  $G_{\parallel}$ . d) Angular divergence, general case. Both an integration over a

range in  $G_{\perp}$  and an uncertainty in  $G_{\parallel}$  result. e) Finite beam diameter. An uncertainty in  $G_{\parallel}$  results that differs for different beams. f) Finite detector aperture. An uncertainty in  $G_{\parallel}$  results that is the same for all beams. In all cases the contributions are greatly exaggerated for illustration.

Fig. 15 Schematic diagrams in real and reciprocal space of the major types of LEED measurements.  $\theta_0$  is the angle of incidence measured from the surface normal,  $\theta$  is the angle the scattered beam makes with the surface normal, and  $\phi$  is the tilt angle of the crystal.

Fig. 16 Schematic diagrams in real and reciprocal space of RHEED measurements. The dashed line in b) indicates the path of the detector, or the deflection of the diffracted beam across a fixed detector.

Fig. 17 Schematic diagram of a fixed-aperture measurement at various energies (an "intensity-vs-energy profile") for a surface that contains randomly distributed steps, illustrating the effect on the fraction of the Bragg intensity that is collected. The solid bar represents the detector aperture. It always has the same solid angle,  $du$ . At an in-phase condition, all of the Bragg intensity is collected. At an out-of-phase condition, a fraction that depends on energy and aperture size is collected. From Ref. 59.

Fig. 18 Schematic diagrams of integrated - intensity-vs-energy measurements at constant momentum transfer. a) Constant azimuthal angle,  $\phi$ , varying colatitude angle,  $\theta_0$ . b) Constant colatitude angle  $\theta_0$ , varying azimuthal angle,  $\phi$ .



Fig. 19 Dependence on  $2M$  of the relative values of the integrals over a Brillouin zone of the Bragg scattering, one-phonon thermal diffuse scattering, and multiphonon scattering. From Ref. 65.

Fig. 20 Generic phase diagram for commensurately adsorbed overlayers and intensity-vs-temperature measurements. The phase diagram plots the allowed phases at any temperature as a function of coverage. I is an ordered phase with a particular structure. L.G. (lattice gas) is the disordered phase. Coexistence regions always occur if the adatoms have an attractive interaction. The dependence of the intensity on temperature at points a, b, and c is indicated schematically. The Debye-Waller factor has been removed. The integral is over the diffracted beam, which at b and c becomes increasingly broad as  $T$  increases. At a, the reflection remains sharp as long as there is any order, and the integral is equal to the peak intensity when measured with a typical instrument.

Fig. 21 Schematic diagram of a LEED diffractometer with Faraday cup and vidicon detectors.

Fig. 22 Schematic diagram of a RHEED diffractometer with light sensitive-diode detector and magnetic-field deflection of diffracted beams. From Ref. 68.

Fig. 23 Comparison of "intensity-vs-energy" profiles for  $W(100)$  taken with a Faraday cup (dashed curve) and with a vidicon detector (solid curve). The two curves are normalized at 80 eV. From Ref. 9.

Fig. 24 Angular-profile measurements of the (01) to (04) beams from GaAs(110) surfaces, a) cleaved in vacuum, b) sputter-etched and annealed. The energy, 180 eV, is near an out-of-phase condition for the stepped surface. The (01) beam is at the right. From Ref. 92.

Fig. 25 Comparison of two angular profiles of the (01) beam from a sputter-etched GaAs (110) surface that has been annealed at two different temperatures; Solid curve: 350°C for 10 min., dashed curve: 560°C for 10 min. Each curve is the average of 30 scans, requiring approximately one minute. The curves are normalized at their maxima. The actual peak intensities differ by a factor of 7. From Ref. 92.

Fig. 26 Two-dimensional angular profile of the (00) reflection from Si(111) at 180 eV. From Ref. 11.

Fig. 27 Contour maps of RHEED profiles taken at two different times after deposition of Ga onto a GaAs (001) surface in the presence of an As background. With increased time the streaks sharpen to spots, demonstrating increasing order in the surface. From Ref. 57.

Fig. 28 Intensity-temperature measurement for the disordering of a saturation-coverage  $W(110) p(2 \times 1)-O$  layer; O: Measured "peak" intensity, intensity corrected for instrument response. The change in width of the angular profile (--) and the instrument response function width (...) are also shown. From Ref. 74.

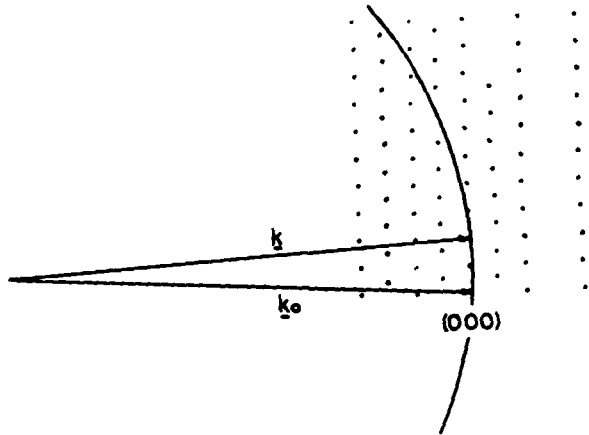
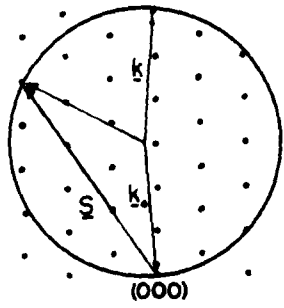
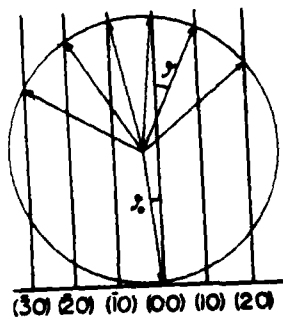
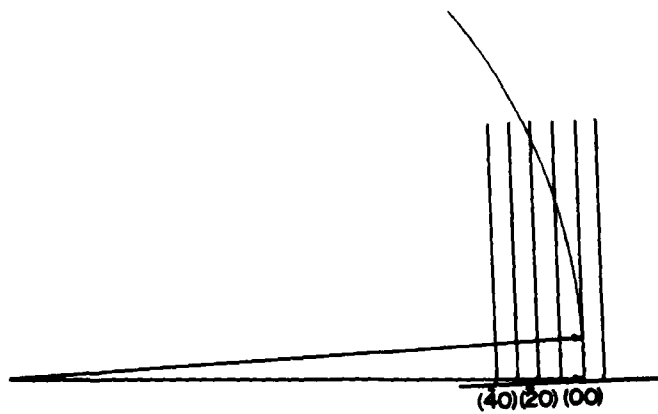


Fig. 1



a)



b)

Fig. 2

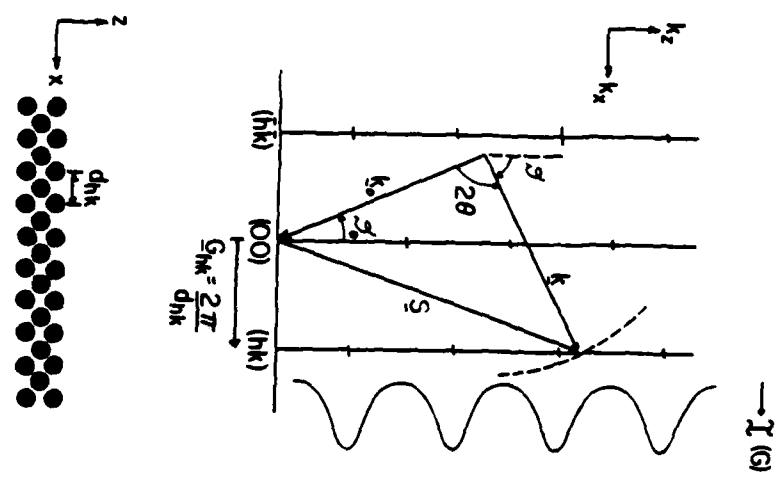


FIG. 3

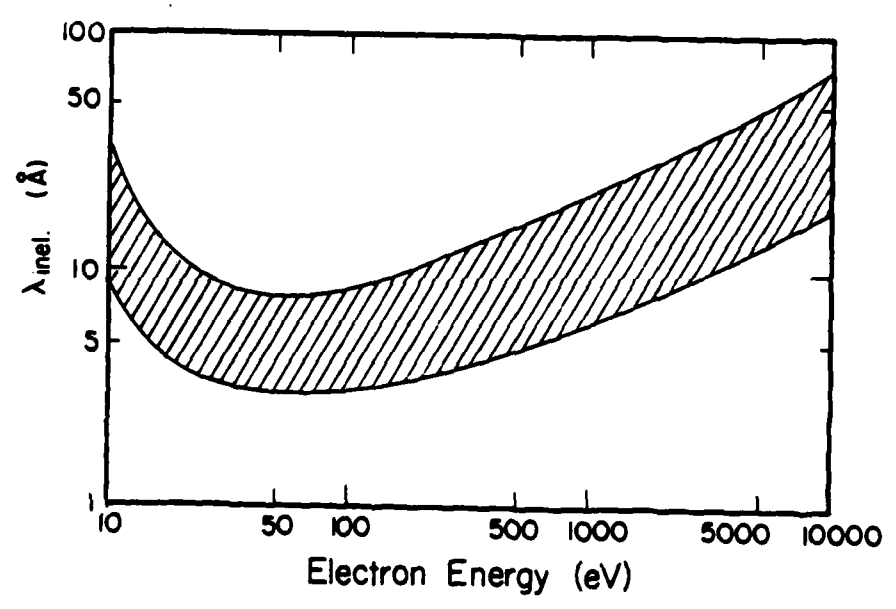


Fig. 4

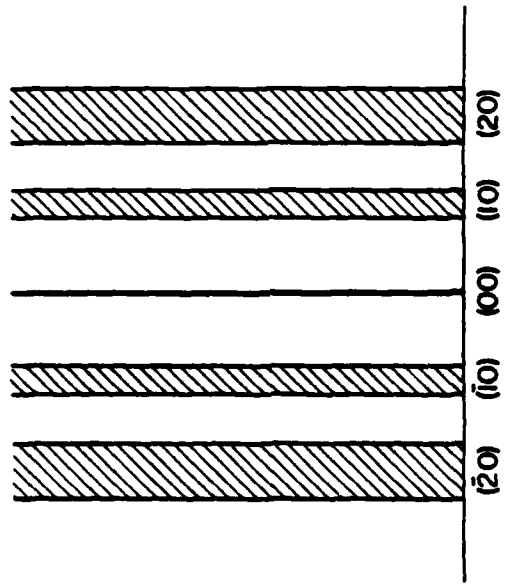
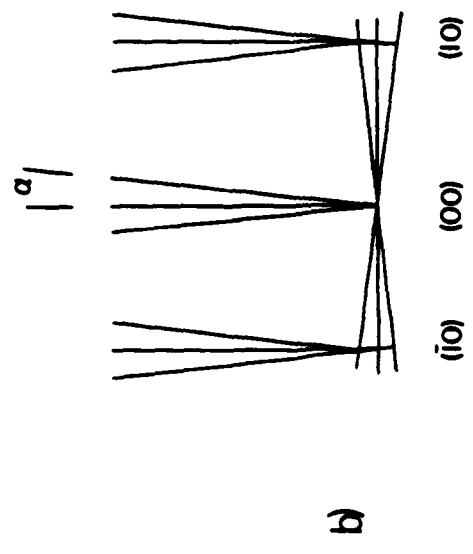
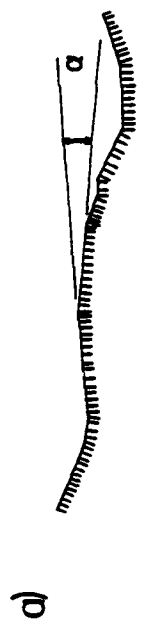


Fig. 5



b)



a)

Fig. 6

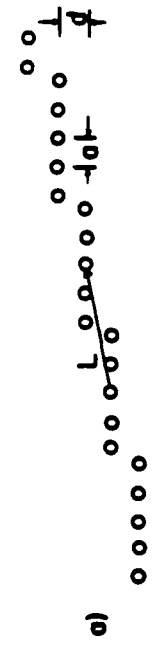
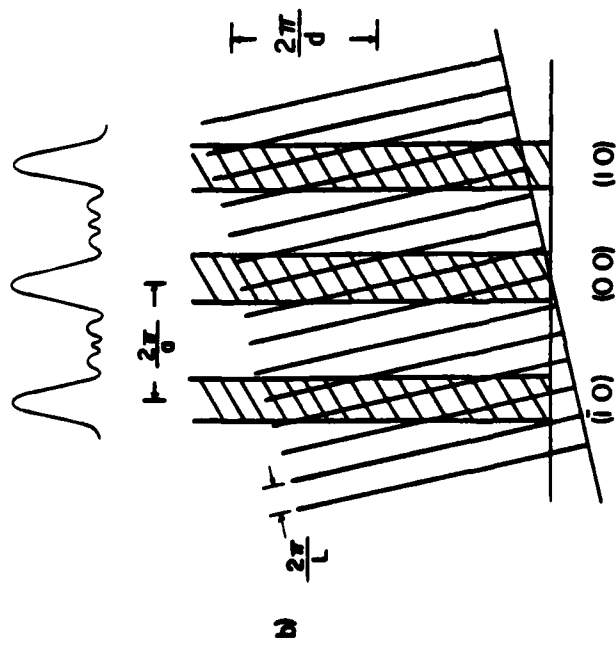


Fig. 7

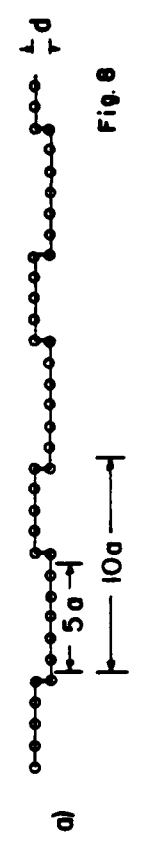
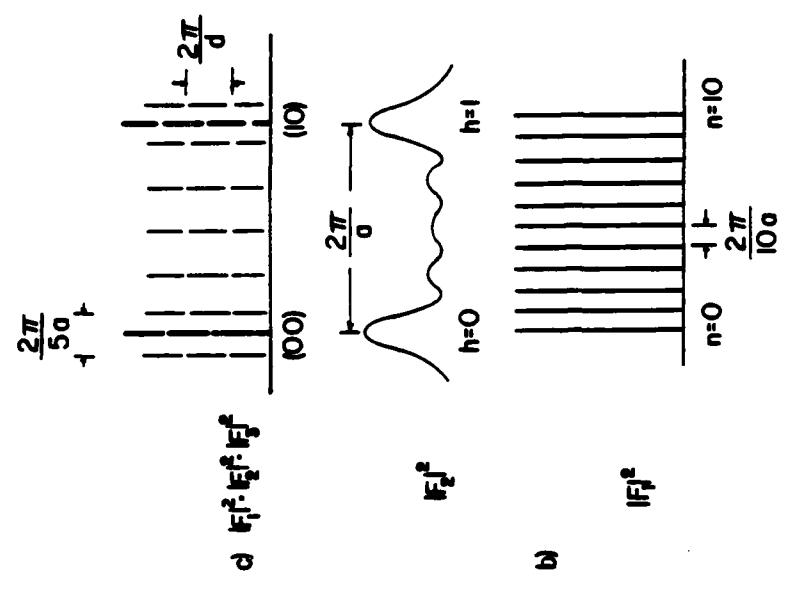
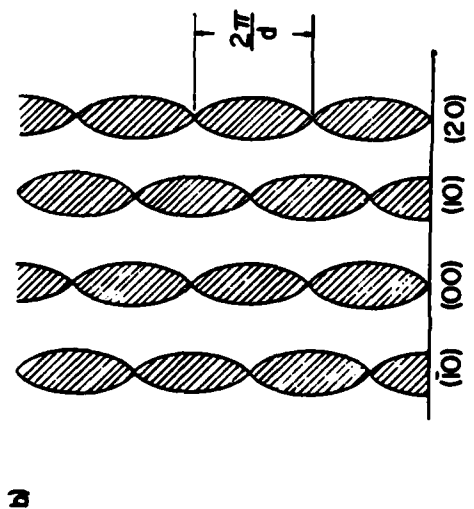
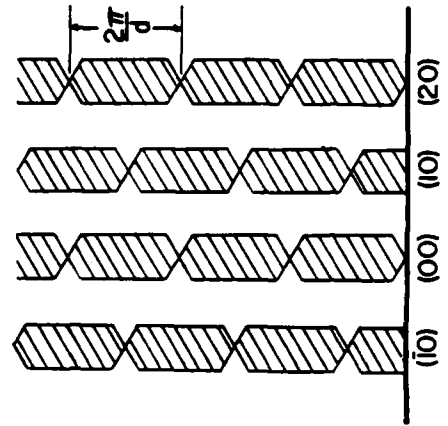


Fig. 8



b)



a)

Fig. 10



Fig. 9

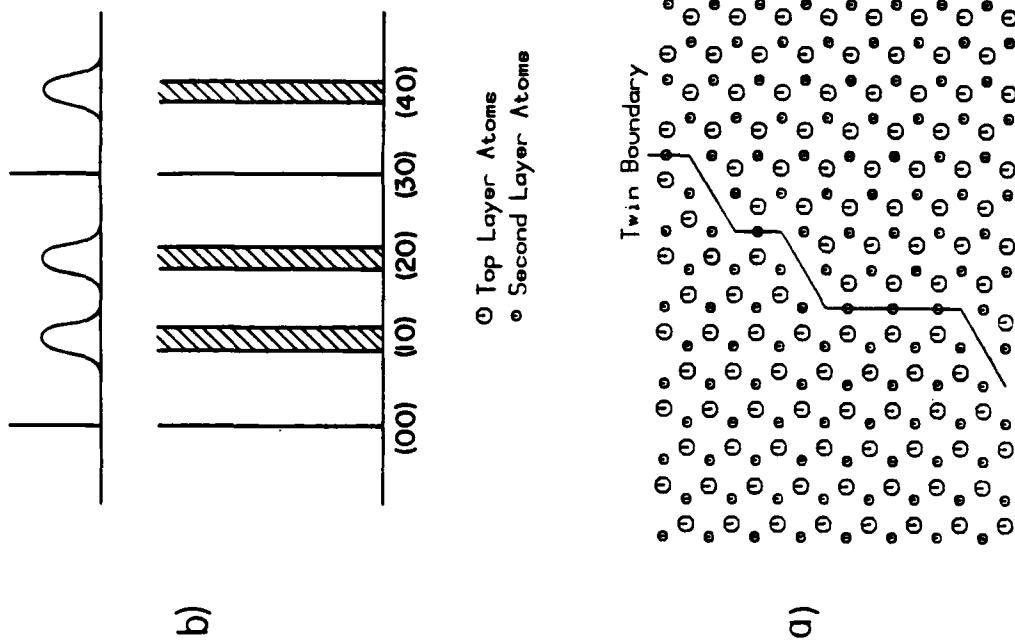


Fig. 11

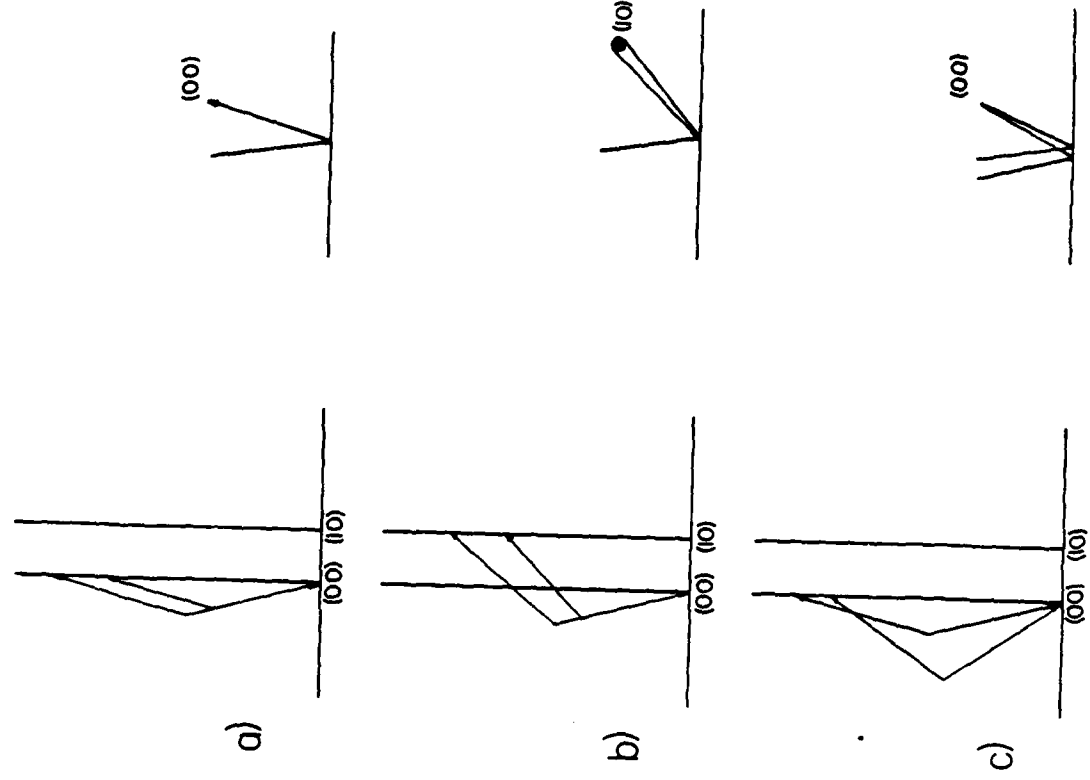
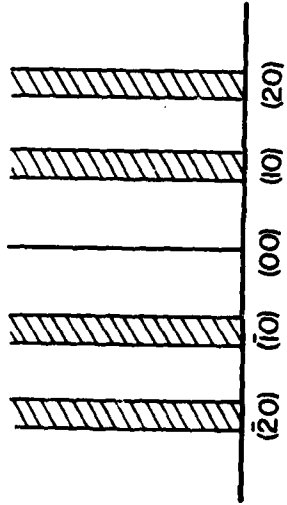
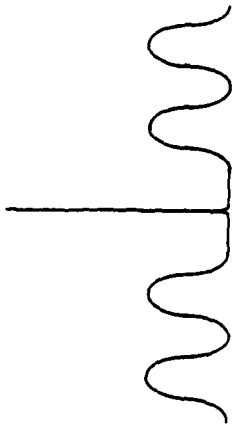


Fig. 13

Fig. 14-1



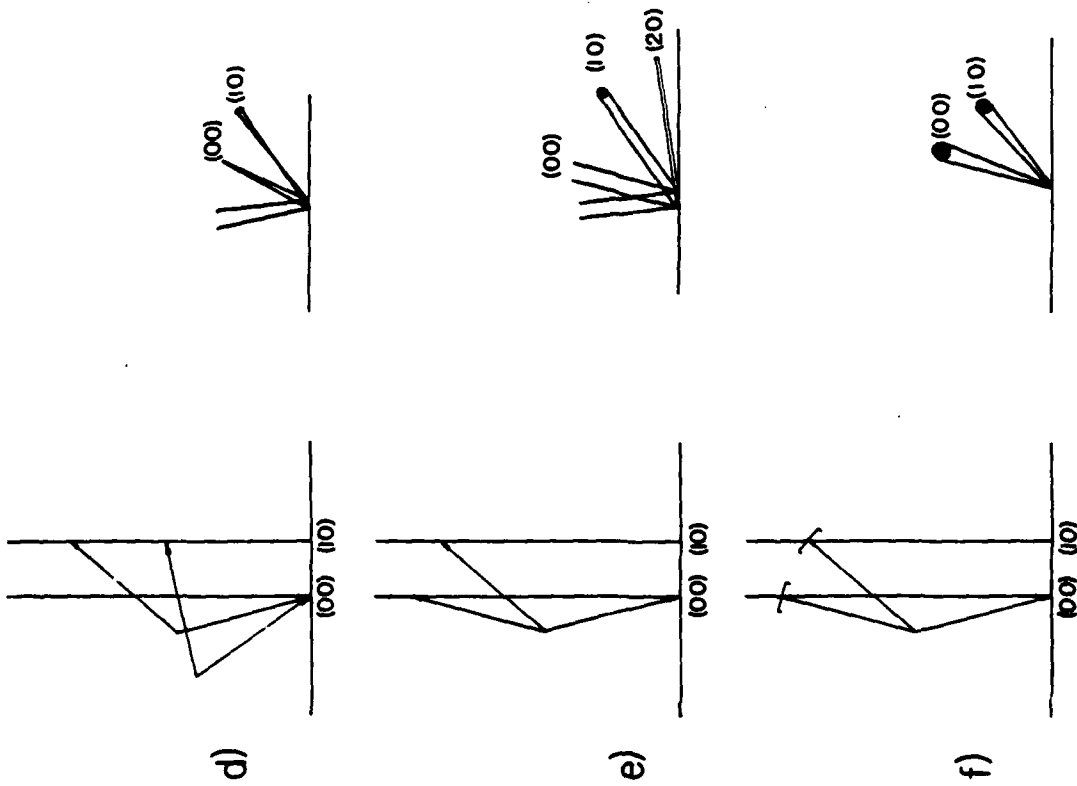
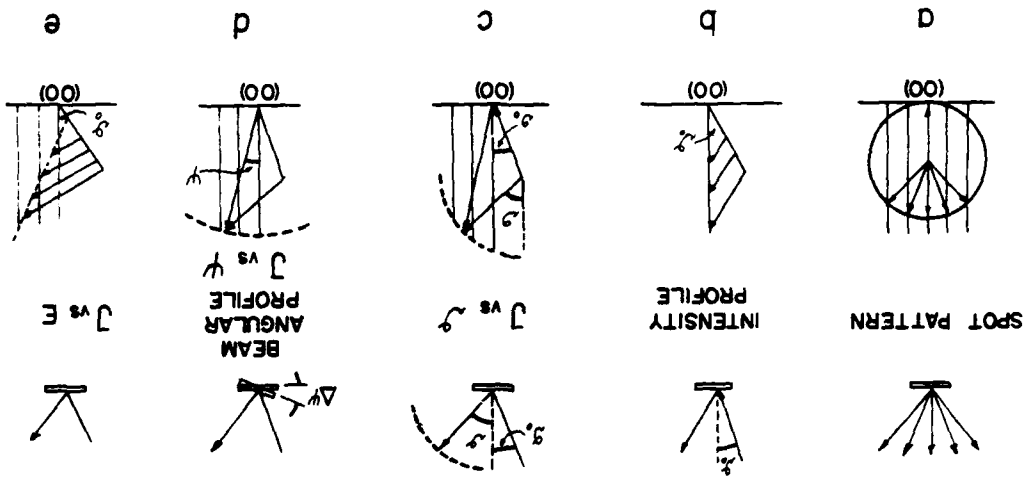
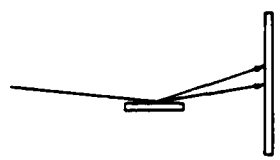
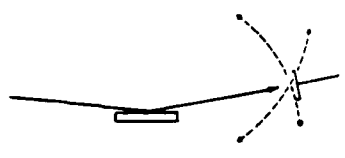


Fig. 14-2



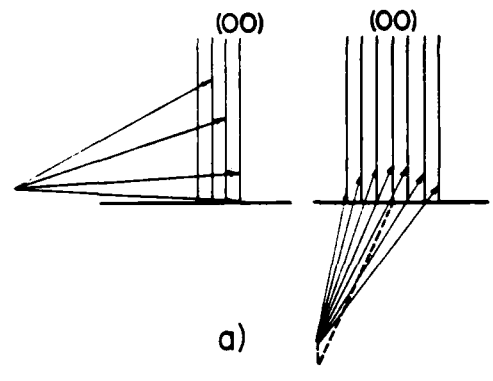
PATTERN



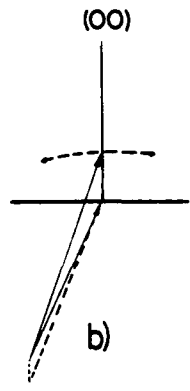
ANGULAR PROFILE



ROTATION PLOTS



a)



b)

c)

Fig. 16

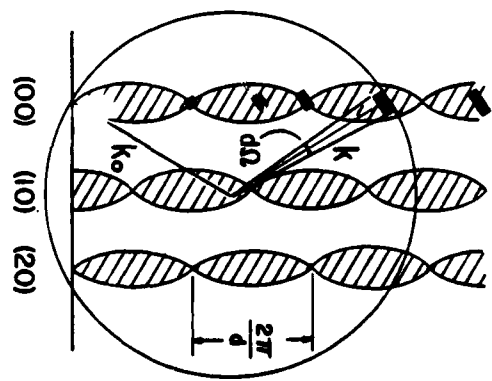


FIG. 17

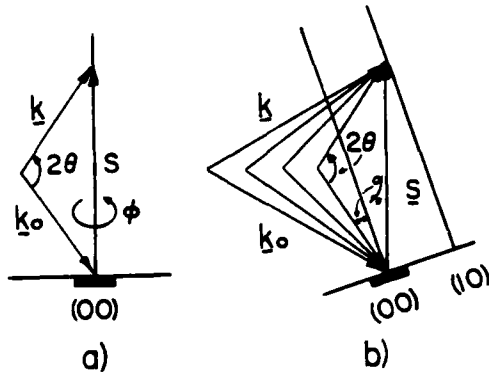


Fig. 18

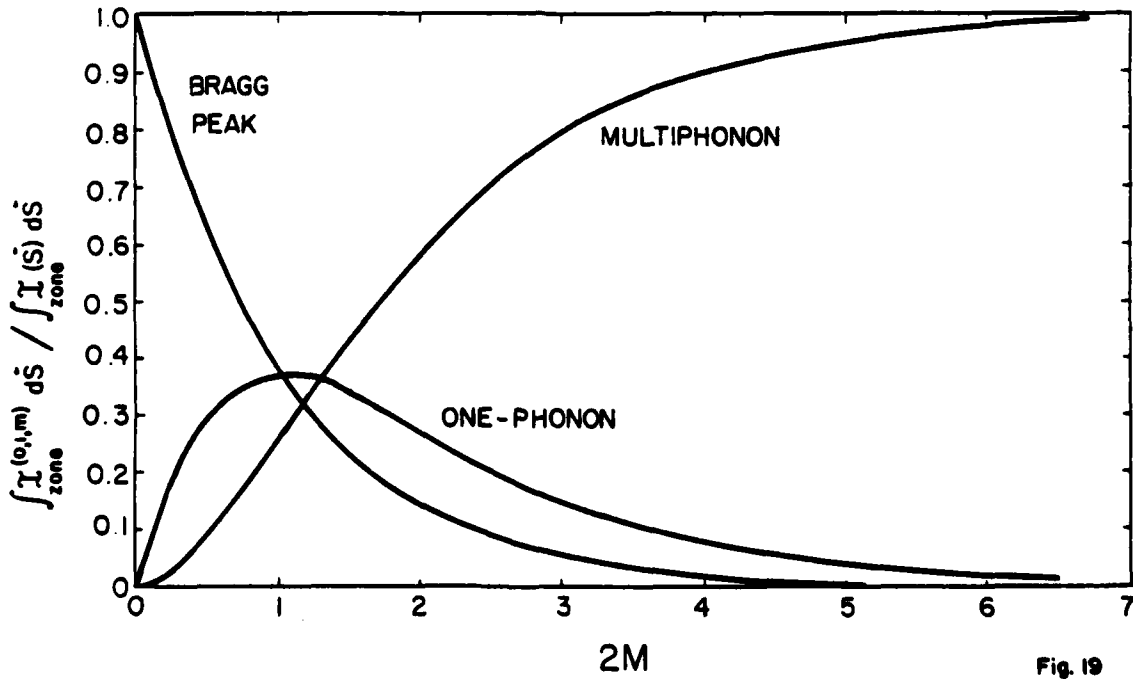


Fig. 19

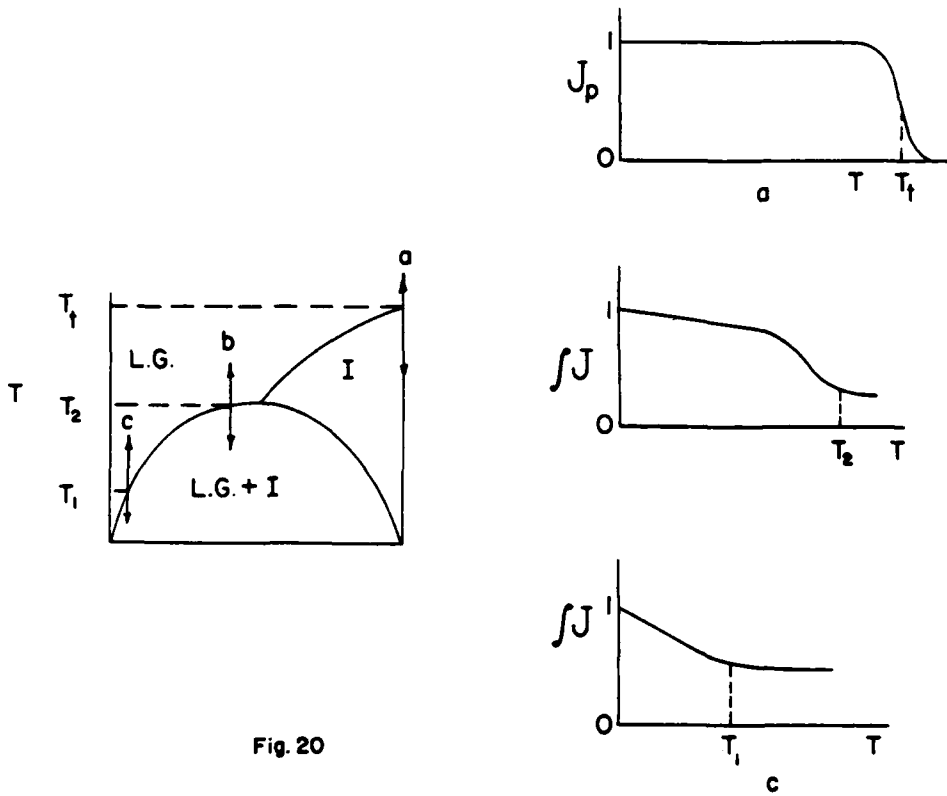


Fig. 20

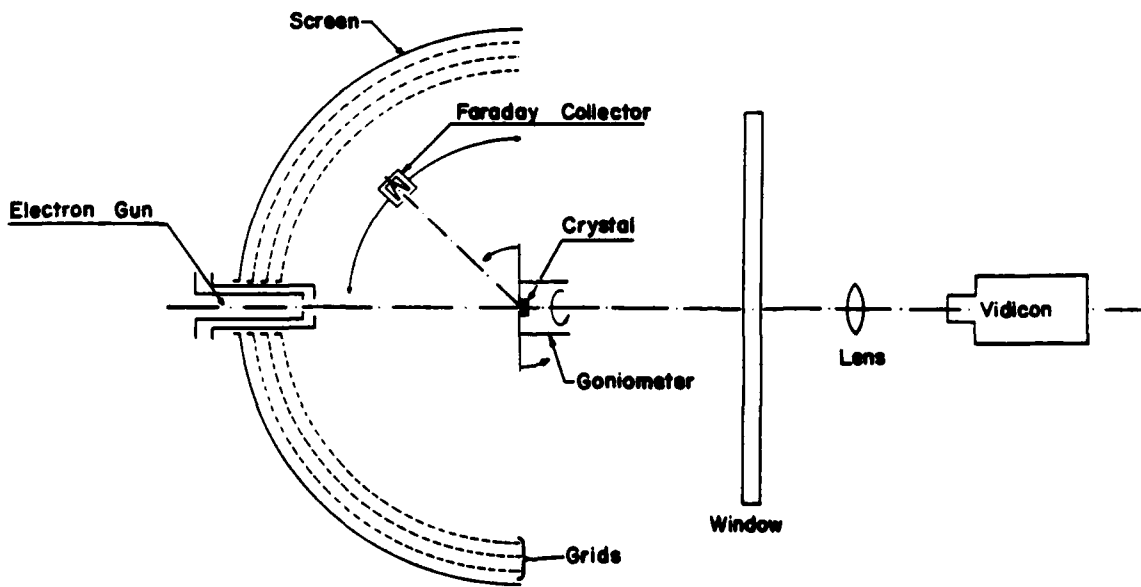


Fig. 21

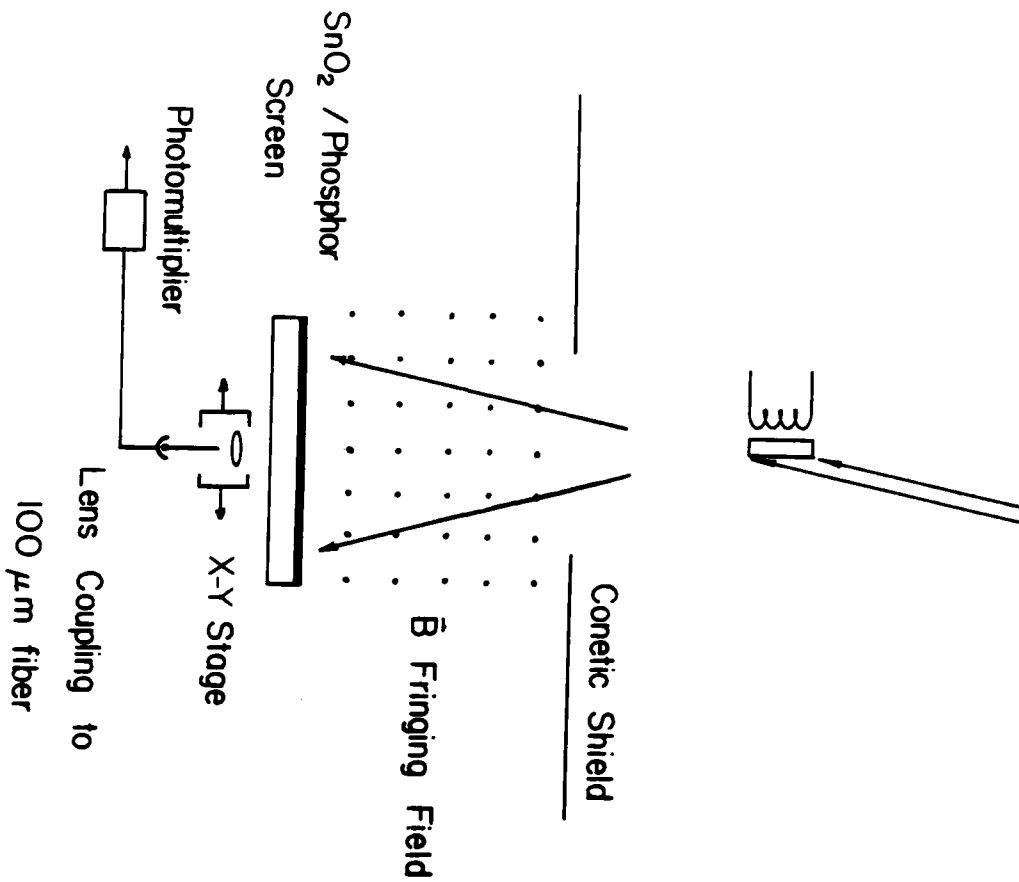


Fig. 22

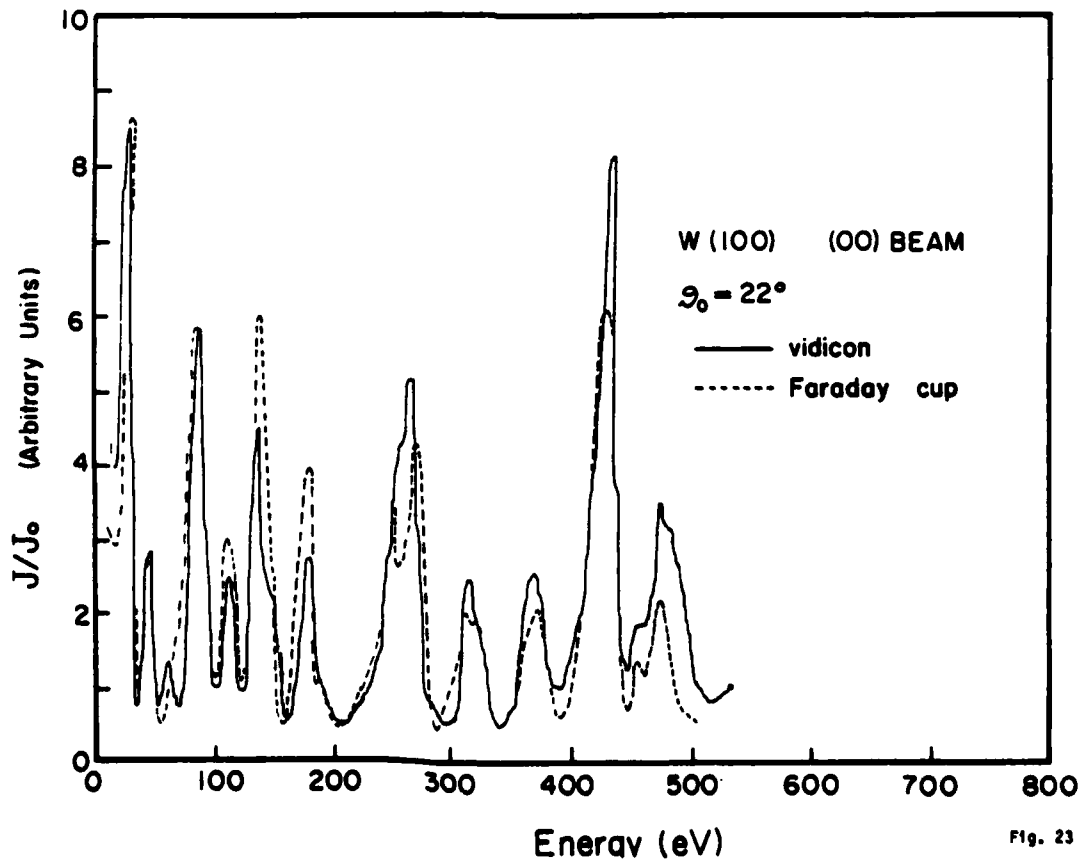


Fig. 23

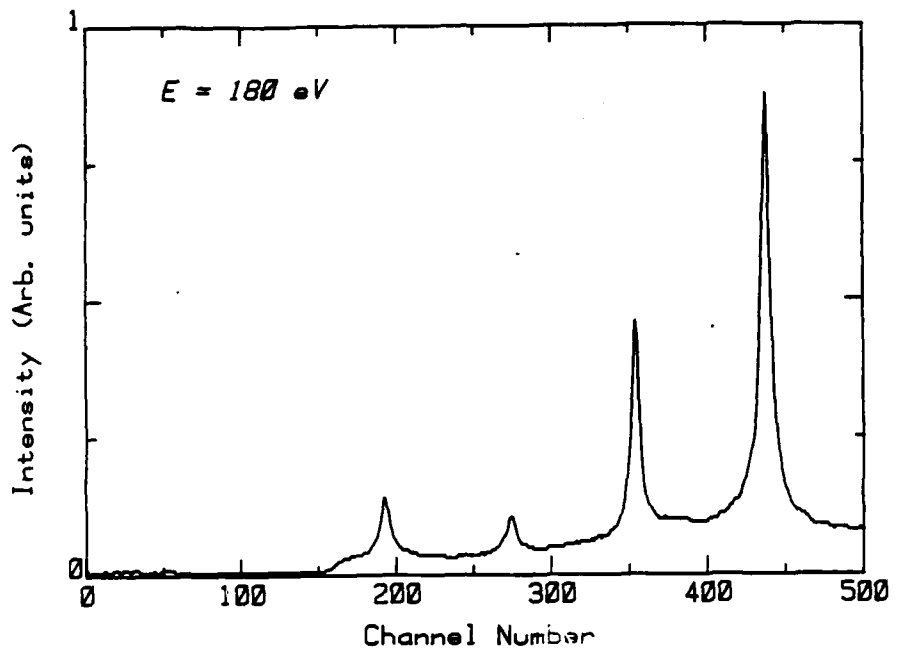


Fig. 24a

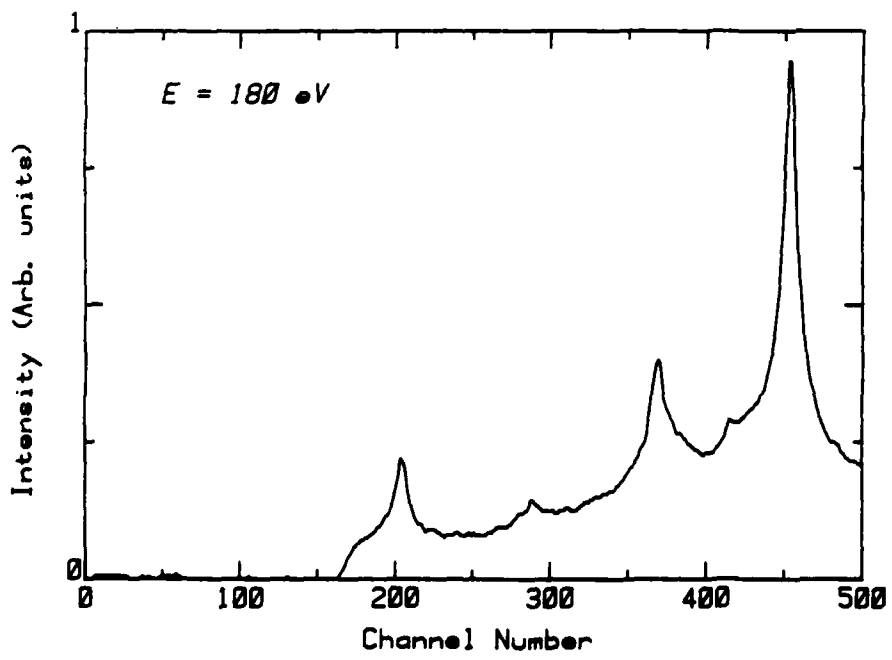


Fig. 24b

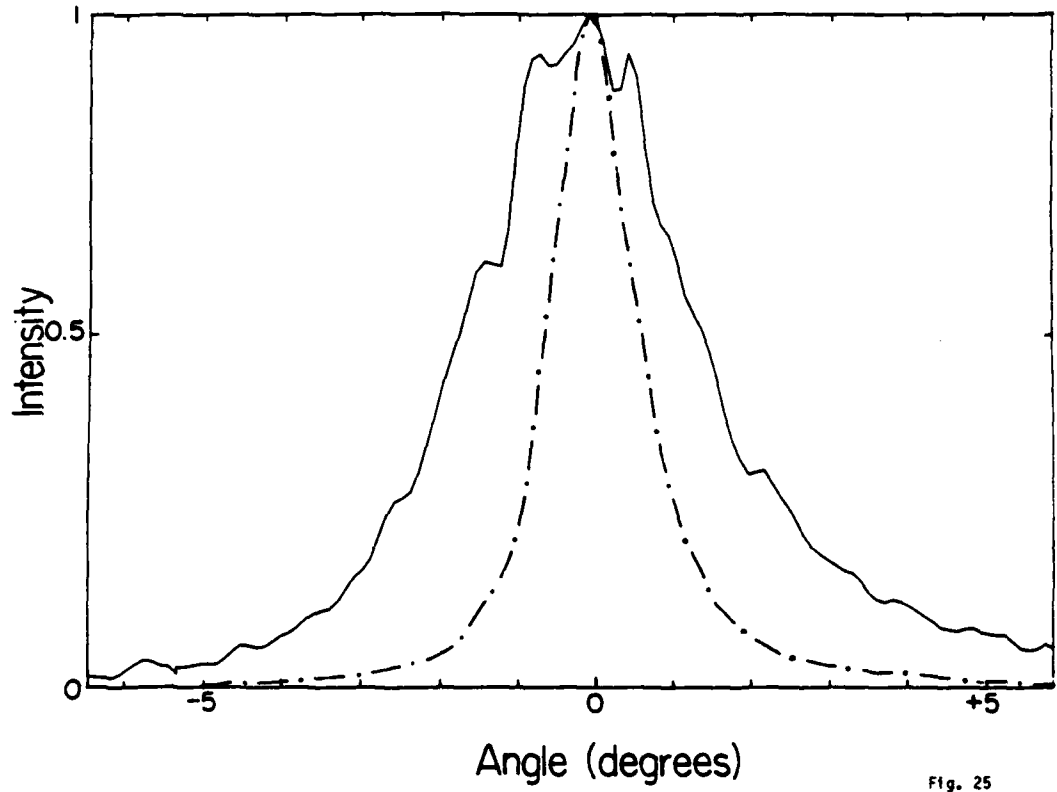


Fig. 25

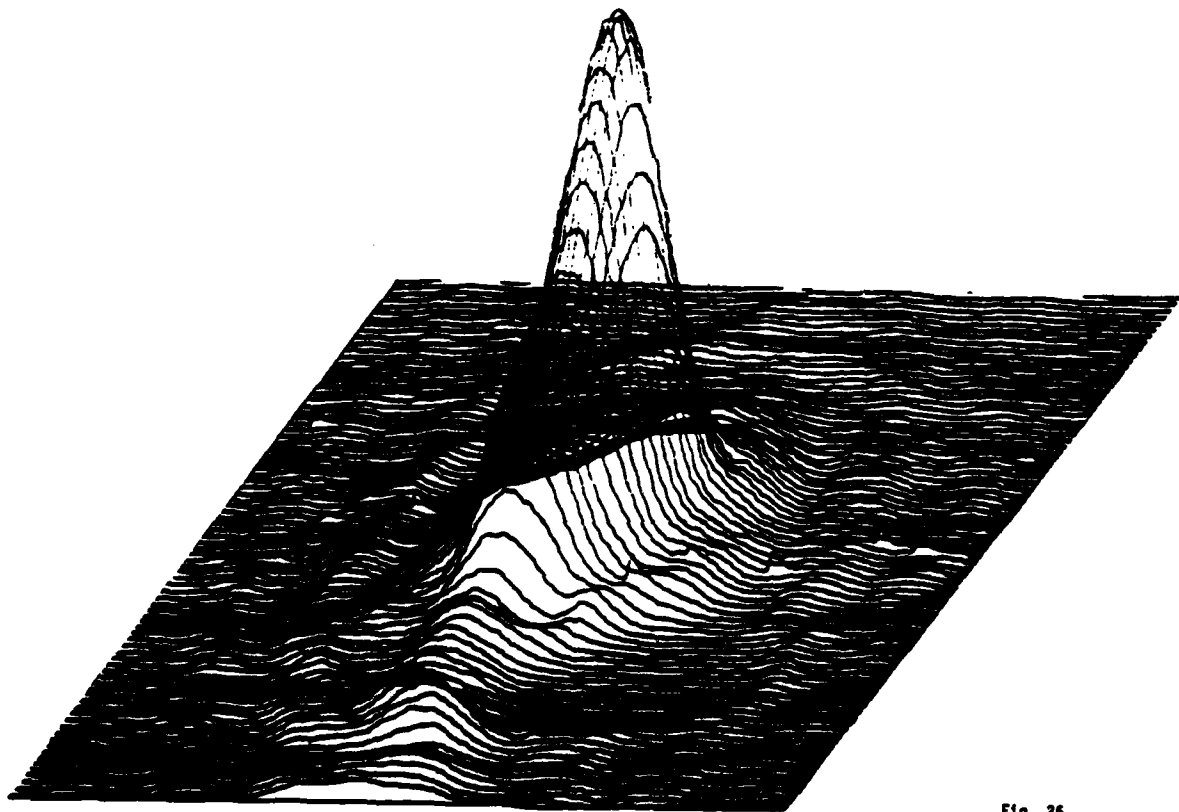


Fig. 26

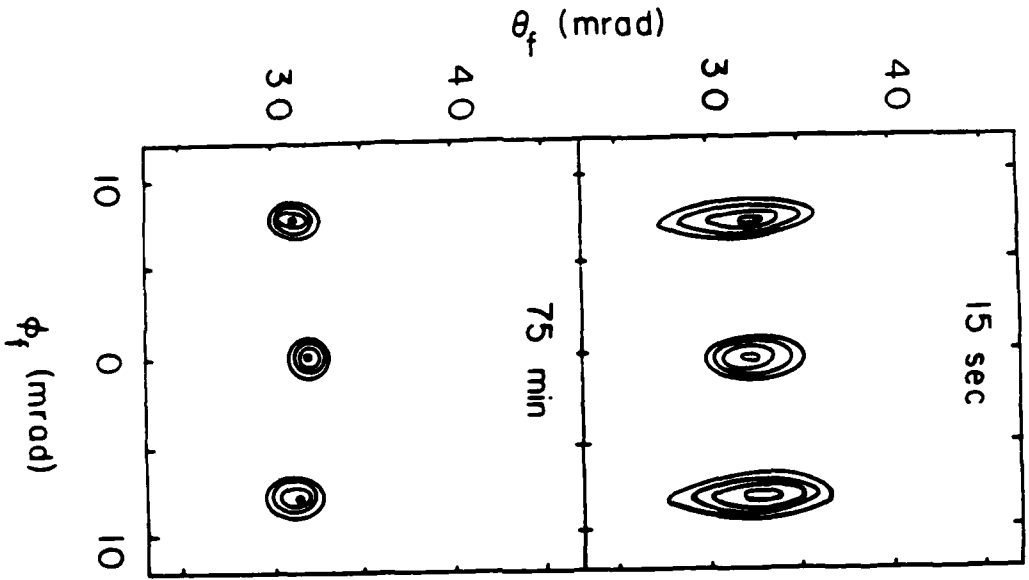


Fig. 27

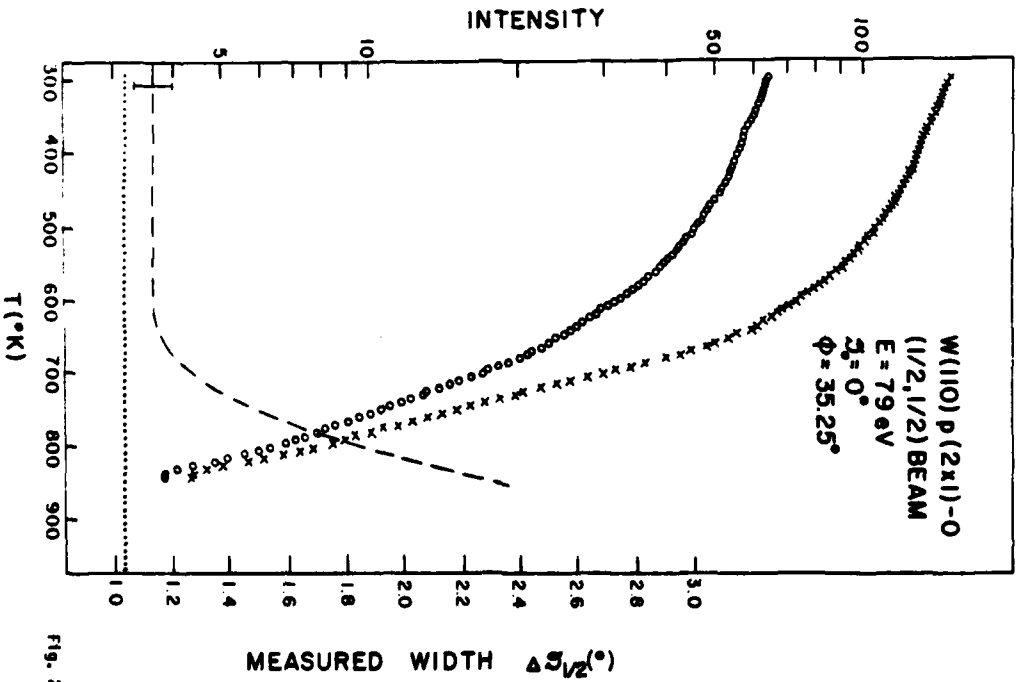


Fig. 28



LMED  
8